

Analytical solutions for multi-stage fractured shale gas reservoirs with damaged fractures and stimulated reservoir volumes

Jie Zeng^{a,*}, Wai Li^{a,1}, Jishan Liu^a, Yee-Kwong Leong^a, Derek Elsworth^b, Jianwei Tian^a, Jianchun Guo^c, Fanhua Zeng^d

^a Department of Chemical Engineering, School of Engineering, The University of Western Australia, 35 Stirling Highway, Perth, WA 6009, Australia

^b Department of Energy and Mineral Engineering, G3 Center and Energy Institute, The Pennsylvania State University, University Park, PA 16802, USA

^c State Key Laboratory of Oil and Gas Reservoir Geology and Exploitation, Southwest Petroleum University, Chengdu 610500, China

^d University of Regina, Petroleum Systems Engineering, Regina, SK S4S 0A2, Canada

ARTICLE INFO

Keywords:

Shale gas reservoir
SRV
Fracture damage

ABSTRACT

After performing hydraulic fracturing in shale reservoirs, the hydraulic fractures and their adjacent rocks can be damaged. Typically, the following fracture damage scenarios may occur: (1) choked fractures; (2) partially propped fractures with unpropped or poorly propped sections at the middle or tail of fractures; (3) fracture face damage; and (4) multiple damage cases. The classical fracture skin factors are derived under steady-state conditions. They are not accurate when the damaged length is relatively long and are not applicable for multiple damage and partially propped fractures. In this article, a new analytical model is established considering all above-mentioned fracture damage mechanisms, complex gas transport mechanisms, and the stimulated reservoir volume (SRV) of shale gas reservoirs.

The matrix model is a spherical element model considering the slip flow, Knudsen diffusion, surface diffusion, and desorption. Natural fractures are idealized as a thin layer that evenly envelops the matrix. The reservoir-fracture flow model is a ten-region linear flow model which can handle fracture damage mechanisms. Specifically, the inner reservoir region is treated as an SRV where the secondary fracture permeability obeys a power-law decreasing trend due to the attenuate stimulation intensity.

This model is validated by matching with the Marcellus Shale production data. And the degraded model's calculation matches well with that of a published linear flow model. New type curves are generated and sensitivity analyses are conducted. Results indicate that the presence of the SRV diminishes pressure and derivative values in certain flow regimes depending on the SRV properties. Different damage mechanisms all control specific flow regimes but the fracture face damage shows the slightest influence. In the multiple fracture damage case, some typical flow regimes can be easily identified except those induced by the partially propped fractures. The field application example further ensures the applicability in dealing with real field data.

1. Introduction

Shale gas reservoirs with ultra-low permeability are generally artificially fractured to obtain economical gas rates. Owing to the ultra-low matrix permeability, fractures serve as the major flow channels for gas production. Unfortunately, during hydraulic fracturing, induced fracture impairment may occur due to various mechanisms including proppant embedment (Guo and Liu, 2012; Liu et al., 2018), fine migrations (Pope et al., 2009), proppant crushing and deformation (Mittal

et al., 2018; Han and Wang, 2014), fracturing fluids leak-off (Ning et al., 1995; Guo and Liu, 2014), proppant backproduction (Parker et al., 1999), proppant diagenesis (LaFollette and Carman, 2010), insufficient proppant injection, proppant over-displacement (Themig, 2010), and stress-induced fracture damage (Valko and Economides, 1993). In this article, the fracture damage of shale gas formations involves the following types. The first type is the choked fracture which has a damaged section at the connection between the horizontal well and the hydraulic fracture. A reduction of fracture permeability or fracture

* Corresponding author.

E-mail address: jie.zeng@research.uwa.edu.au (J. Zeng).

¹ The first two authors contributed equally to this work.

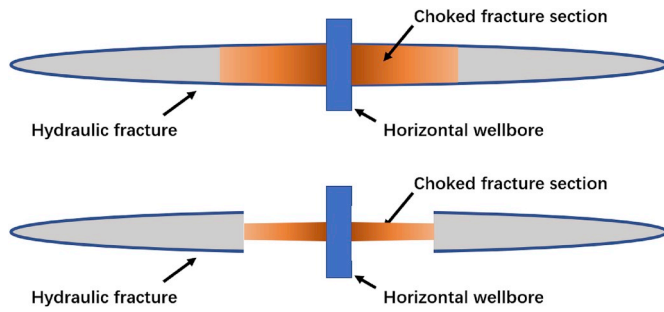


Fig. 1. Schematic of choked fractures (plan view).

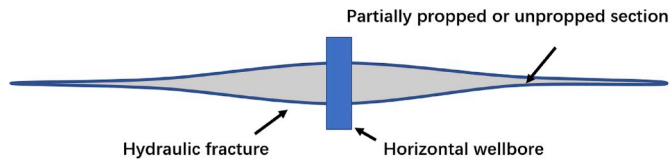


Fig. 2. Schematic of a partially propped fracture (plan view).

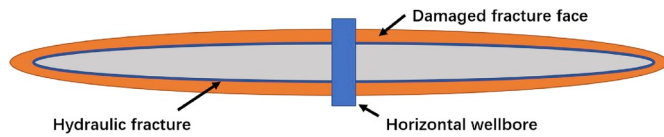


Fig. 3. Schematic of fracture face damage (plan view).

width can occur in the damaged section, as shown in Fig. 1. Proppant backproduction and over-displacement are the main causes of this damage (Romero et al., 2003) while proppant embedment and crushing can be possible reasons as well. The second type refers to the partially propped fracture with an insufficiently propped or unpropped section and an undamaged near-wellbore region within the fracture, as shown in Fig. 2. It can result from the undesired proppant distribution and placement, proppant embedment and crushing, and insufficient proppant injection and is heavily influenced by the hydraulic fracture geometry. The third type is the fracture face damage which involves a damaged region at the fracture face, as shown in Fig. 3. Common causes of this damage include fracturing fluids leak-off, polymer impairment, the phase change near fractures, and stress effects (Romero et al., 2003; Reinicke et al., 2013). Moreover, the above-mentioned damage mechanisms may co-exist in a multi-stage fractured horizontal well (MFHW), which refers to multiple fracture damage.

Actually, damaged fracture height caused by stress effects is also a fracture damage mechanism. Here, we treat these fractures as partially penetrating fractures which can be handled by our model as well. Although we know well about the damage mechanisms, how they affect the pressure and rate responses of a fractured shale gas reservoir has not been fully understood. In the literature, skin factors have been widely used to simulate fracture damage in well testing and production. Cinco-Ley and Samaniego (1977) established a model which is modified from a finite conductivity fracture model to include wellbore storage and fracture damage. Their study reveals that the fracture face damage can be estimated from the early-time well responses through type-curve matching. Then, Cinco-Ley and Samaniego (1981) further considered the effects of choked fracture damage on the transient pressure behavior and analyzed different pressure responses between finite-conductivity and damaged fractures. Azari et al. (1991) presented how choked fracture damage controls the well performances of constant-pressure production cases. Results show that it impairs the productivity of wells with high-conductivity fractures more significantly. Wang et al. (2000) studied the fracture face skin effects caused by the liquid condensate in

gas-condensate reservoirs. They concluded that the productivity of fractured gas-condensate wells experiences a dramatical reduction due to this tantamount fracture face skin. Romero et al. (2003) used a direct boundary element method (BEM) to investigate the influence of fracture face skin and choked fracture skin on fractured well performances. Results indicate that the nonuniform fracture face skin significantly reduces the dimensionless productivity index while choked fractures' effects are less complex and can be addressed through an apparent drop of the proppant number. The stress-induced fracture face skin was examined by Reinicke et al. (2013). They pointed out that the mechanical interaction between rocks and proppants can cause a permeability reduction up to 90% at the fracture face. However, the fundamental equations of skin factors are derived under the steady state and are accurate when the damaged-zone length is relatively small (Cinco-Ley and Samaniego, 1977). Moreover, the pressure and rate behavior of dual-porosity shale reservoirs under multiple fracture damage conditions or partially propped fracture conditions cannot be analyzed through traditional skin factors. Recently, linear flow models were derived to handle only the fracture face skin under unsteady state conditions (Miao et al., 2019; Wu et al., 2019). For partially propped fractures, Qin et al. (2018) developed a double-segment fracture model which considers the damaged fracture effective length caused by fracture closure and can interpret effective fracture properties and identify fracture closure. However, that model is only applicable for infinite reservoirs and is not suitable for more complex fracture damage cases. For multiple fracture damage, Zeng et al. (2019) developed a single-porosity composite linear-flow model. However, that model is too simple to deal with dual-porosity shale formations with SRVs and complex gas transport mechanisms. And the flow regimes of dual-porosity shale formations with SRVs are significantly different from those of a single-porosity reservoir. Until now, no effective and simple method has been proposed to evaluate complex fracture damage circumstances of shale gas formations.

Apart from fracture damage, the existence of newly generated large fracture networks has been observed and evidenced by microseismic mapping in many shale reservoirs (Mayerhofer et al., 2010). The properties of the SRV are key parameters for post-fracturing performances. The induced fracture network size can be treated as a 3-D volume and is dependent on the rock properties and the injected fracturing-fluid volume (Mayerhofer et al., 2010). Within the SRV, the stimulation intensity decreases along the fracture branch propagation direction, which leads to the fracture network transport property variation (Wang et al., 2015b). In the literature, many researchers used power-law expressions to depict fracture network property variations in the fluid-flow direction, as shown below (Chang and Yortsos, 1990; Acuna et al., 1995; Wang et al., 2015b; Fan and Ettehadtavakkol, 2017a, 2017b)

$$k_{fSRV}(y) = k_0 \left(\frac{y}{y_{ref}} \right)^{H-E-\theta}, \quad (1)$$

$$\phi_{fSRV}(y) = \phi_0 \left(\frac{y}{y_{ref}} \right)^{H-E}, \quad (2)$$

where H is the mass fractal dimension; E is the Euclidean dimension; θ is the fractal exponent which increases with higher fracture network tortuosity and poorer connectivity; y is the flow direction coordinate; y_{ref} is the reference length of the power-law equation in ft; k_{fSRV} is the fracture network permeability that changes along the flow direction in md; k_0 is the permeability at y_{ref} in md; ϕ_{fSRV} is the fracture network porosity; ϕ_0 is the porosity at y_{ref} . Fan and Ettehadtavakkol (2017a) validated the induced fracture network property power-law distribution by matching the power-law fracture distribution with Barnett Shale microseismic fracture density data. To obtain analytical solutions, we follow the assumption of Fan and Ettehadtavakkol (2017b) and assume $H = E$.

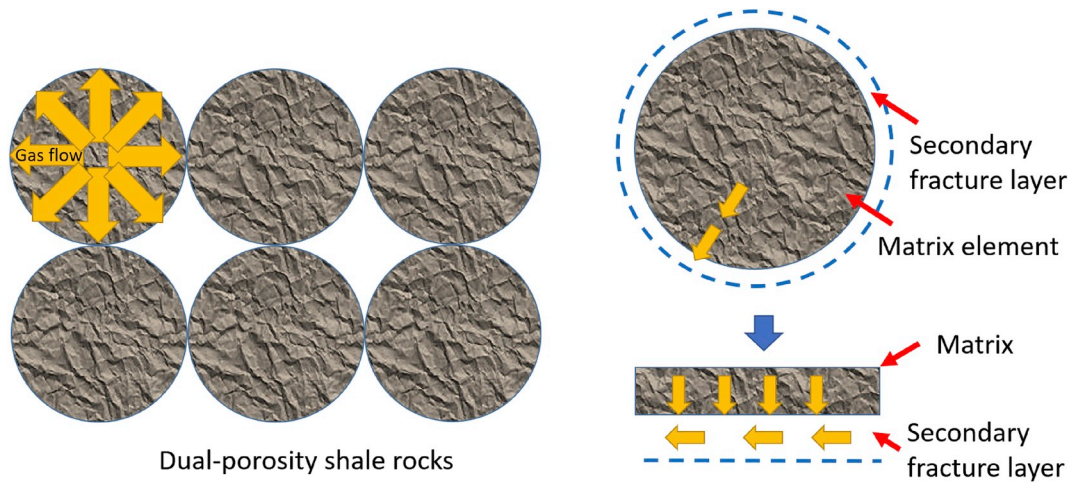


Fig. 4. Schematic of the matrix flow model.

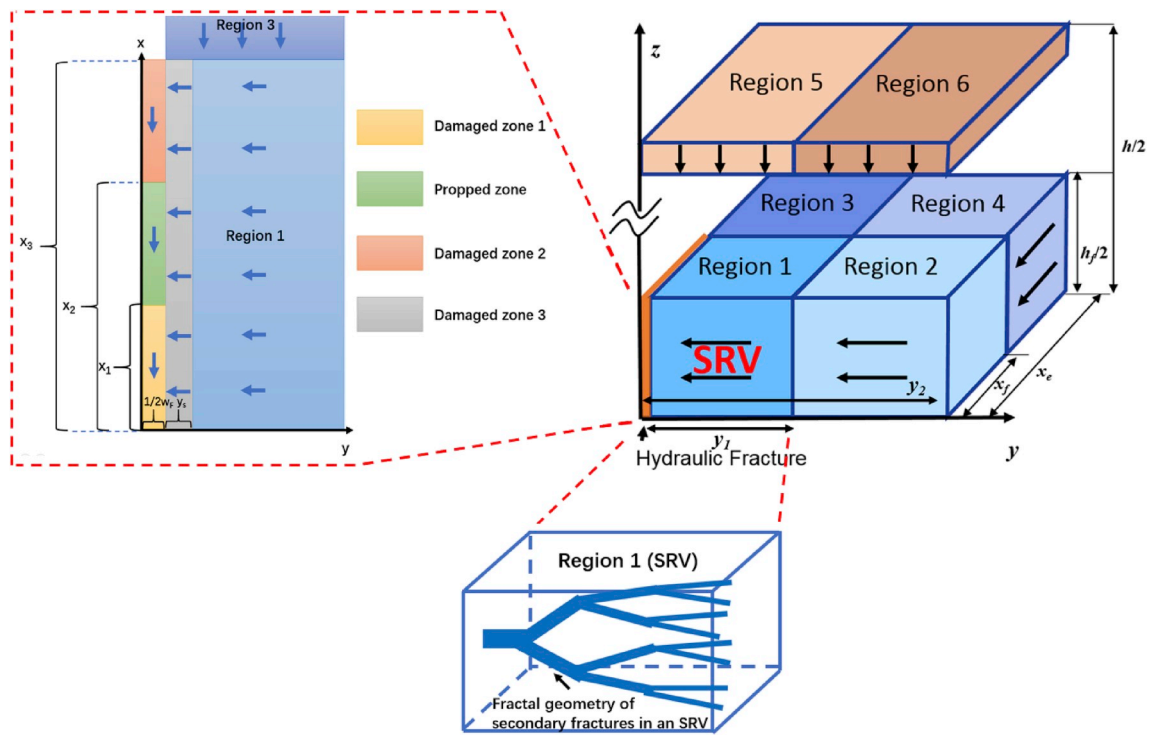


Fig. 5. Schematic of the reservoir-fracture linear flow model (modified from Fan and Ettehadtavakkol, 2017a; Zeng et al., 2019).

Consequently, $k_{fSRV}(y) = k_f(y/y_s)^{-\theta}$ and $\phi_{fSRV}(y) = \phi_f$. Here y_s is the reference length which is the sum of fracture face invaded thickness and half-fracture width in ft. Fan and Ettehadtavakkol (2017b) assumed that the unstimulated reservoir volume (USRV) is single-porosity, which can underestimate the contribution of USRVs as they are naturally fractured. The aforementioned literature review has revealed several gaps in modeling shale gas production with damaged hydraulic fractures. This research aims at establishing a more general analytical model that considers special features of stimulated shale gas reservoirs and complex fracture damage and uncovering how SRV properties and different fracture damage mechanisms affect the responses of MFHWs in shale gas plays.

2. Conceptual models

In this section, the conceptual models and the assumptions used to develop the mathematical models are introduced. The reservoir is a box-shaped shale gas reservoir with closed outer boundaries. The MFHW is drilled at the center of the reservoir. To effectively describe the artificially fractured shale reservoir, we utilize three distinct porous systems: the matrix, natural (secondary) fractures, and hydraulic fractures. As indicated in Figs. 4 and 5, the spherical flow in shale matrix elements and the composite linear flow in the reservoir-fracture system are considered. For matrix gas flow modeling, an improved model that takes into account the slip corrected flow, Knudsen diffusion, surface diffusion, desorption, and real-gas effects is employed. Following de Swaan-O's model (de Swaan, 1976), the matrix gas moves from the inner spherical block to its surface. The secondary fracture system is idealized as a constant-thickness layer that envelopes the spherical blocks. Due to

the relatively high permeability of secondary fractures, the matrix gas is instantaneously and evenly distributed in 1/2 of the secondary fracture layer volume (Ozkan et al., 2010). After entering secondary fractures, the gas flow turns into 1-D linear flows in each reservoir-fracture flow region. Fig. 5 illustrates the composite linear flow model with ten linear-flow regions for the reservoir-fracture system. Regions 5 and 6 serve as the reservoir volume beyond the hydraulic fracture height with 1-D vertical flows. Regions 3 and 4 represent the reservoir volume beyond the hydraulic fracture tip with 1-D flows in the x-direction. The height of the two regions equals the hydraulic fracture height. And regions 2 and 1 are the inner reservoir blocks representing the USRV and the SRV respectively with 1-D flows in the y-direction. Particularly, four sub-regions are applied to handle complex fracture damage. Damaged zone 3 is suitable for fracture face damage. Damaged zone 2 is designed for partially propped or unpropped sections. One can also change the propped zone properties to simulate the partially propped or unpropped section in the middle of a fracture. And damaged zone 1 can deal with choked fractures. Therefore, it is flexible and easy to model complex and multiple fracture damage with these sub-regions. Flows in different flow regions are coupled via flux and pressure continuity conditions at their interfaces. Other assumptions include:

- (1) The reservoir is isothermal with single gas-phase flows. The gas flow in the matrix involves complex transport mechanisms (slippage, Knudsen diffusion, surface diffusion, desorption, and real-gas effects) while the gas flow within fractures simply obeys Darcy's law.
- (2) A cased-hole completion is applied to the MFHW, therefore, the fluids flow into the wellbore through hydraulic fractures only. Gravity effects are ignored due to the single-phase flow condition and the extremely tight texture of shale rocks.
- (3) The MFHW can produce under either a constant-rate condition or a constant-pressure condition.
- (4) Due to the symmetry, 1/8 of a fracture drainage volume is selected to derive the mathematical models, as shown in Fig. 5.

3. Mathematical models

In this section, the mathematical models and their analytical solutions are outlined. For convenience, the analytical solutions are all demonstrated in the Laplace domain in the dimensionless form. Here, the definition of dimensionless variables is introduced first.

The dimensionless pseudopressure is defined as

$$p_{pD} = \frac{k_{ref} h_{ref}}{1422 q_{Fi} T} [p_p(p_i) - p_p(p)], \quad (3)$$

where q_{Fi} is the total flow rate of the MFHW in Mscf/D; T is the temperature in °R; k_{ref} is the reference permeability for the dimensionless variable definition in md; h_{ref} is the reference height in ft; p_p is the pseudopressure in psi^2/cp ; p_i is the initial reservoir pressure in psi; and p is the pressure in psi. The pseudopressure is expressed by the following equation (Ozkan et al., 2010; Al-Hussainy and Ramey, 1966)

$$p_p(p) = 2 \int_{p_{ref}}^p \frac{k}{k_i} \frac{p}{\mu_g Z} dp, \quad (4)$$

where μ_g is the gas viscosity in cp; p_{ref} is the reference pressure in psi; k and k_i are permeability and initial permeability in md; and Z is the Z-factor. The dimensionless time is expressed as

$$t_D = \frac{\eta_{ref} t_a}{d_{ref}^2}, \quad (5)$$

where d_{ref} is the reference length in ft; η_{ref} is the reference diffusivity in ft^2/hour ; and t_a is the pseudotime in hour and is given by Anderson and Mattar (2007).

$$t_a = \mu_{gi} c_{ti} \int_0^t \frac{dt}{\tilde{\mu}_g \tilde{c}_i}. \quad (6)$$

Here, $\tilde{\mu}_g$ and \tilde{c}_i are gas viscosity and total compressibility under the average pressure condition in cp and psi^{-1} respectively; and μ_{gi} and c_{ti} are gas viscosity and total compressibility under the initial condition in cp and psi^{-1} . We use the pseudopressure and pseudotime to linearize the diffusivity equations (Ozkan et al., 2010; Anderson and Mattar, 2007). The dimensionless distances in the x-direction are written as

$$x_{1D} = x_F / d_{ref} = x_3 / d_{ref}, \quad (7)$$

$$x_{FD1} = x_1 / d_{ref}, \quad (8)$$

$$x_{FD2} = x_2 / d_{ref}, \quad (9)$$

$$x_{eD} = x_e / d_{ref}, \quad (10)$$

where x_F and x_3 are the hydraulic fracture length in ft; x_2 is the distance from the wellbore to damaged zone 3 in ft; x_1 is the choked section length in ft; x_e is the half reservoir width in ft; and x_{1D} , x_{FD2} , x_{FD1} , and x_{eD} are their corresponding dimensionless length. The dimensionless distances in the y-direction include

$$y_{1D} = y_1 / d_{ref}, \quad (11)$$

$$y_{2D} = y_2 / d_{ref}, \quad (12)$$

$$y_{sD} = (y_s + w_F / 2) / d_{ref}, \quad (13)$$

$$w_D = w_F / d_{ref}, \quad (14)$$

where w_F is the hydraulic fracture width in ft; y_s is the thickness of the damaged fracture face in ft; y_1 is the half SRV width in ft; y_2 is the half fracture spacing in ft; and w_D , y_{sD} , y_{1D} , and y_{2D} are their corresponding dimensionless length. For the z-direction, we have

$$z_{1D} = z_1 / d_{ref} = h_F / (2d_{ref}), \quad (15)$$

$$z_{2D} = z_2 / d_{ref} = h / (2d_{ref}), \quad (16)$$

where h_F is the fracture height in ft; h is the reservoir height in ft; z_1 is the half fracture height in ft; z_2 is the half reservoir height in ft; and z_{1D} and z_{2D} are the dimensionless expressions of z_1 and z_2 . In the spherical flow direction, we also have

$$r_D = r / d_{ref} \quad (0 \leq r \leq r_m), \quad (17)$$

where r is the distance from the location we study to the spherical element center in ft; r_D is the dimensionless form of r ; and r_m is the matrix element radius in ft. The diffusivity terms are given by

$$\eta_{ref} = \frac{2.637 \times 10^{-4} k_{ref}}{\phi_{ref} \mu_{ref} c_{ref}}, \quad (18)$$

$$\eta_{mn} = \left(\frac{2.637 \times 10^{-4} k_{appm}}{\phi_m \mu_{mgi} c_{appmi}} \right)_n, \quad (19)$$

$$\eta_{fi} = \left(\frac{2.637 \times 10^{-4} k_f}{\phi_f \mu_{fji} c_{fji}} \right)_n, \quad (20)$$

$$\eta_{Fn} = \left(\frac{2.637 \times 10^{-4} k_F}{\phi_F \mu_{Fgi} c_{Fi}} \right)_n, \quad (21)$$

where the subscript *ref* is for reference variables; *app* is for apparent variables; *m* represents matrix properties; *i* is for parameters under the initial condition; *f* describes secondary fracture properties; *F* describes

hydraulic fracture properties; and n indicates the n -th region. According to Ozkan et al., (2010), $\eta_{mn} \approx \eta_{mni}$. The dimensionless expressions of them are

$$\eta_{mDn} = \eta_{mn} / \eta_{ref}, \quad (22)$$

$$\eta_{fDn} = \eta_{fn} / \eta_{ref}, \quad (23)$$

$$\eta_{FDn} = \eta_{Fn} / \eta_{ref}. \quad (24)$$

3.1. Matrix flow models

After defining the dimensionless variables, we formulate the conceptual models in this section. The mass balance for the spherical matrix flow can be expressed as

$$-\frac{1}{r^2} \frac{\partial}{\partial r} (r^2 \rho_{mg} v_m) = \frac{\partial (\rho_{mg} \phi_m)}{\partial t} + \frac{\partial [(1 - \phi_m) \rho_{scg} V_{Esc}]}{\partial t}, \quad (25)$$

where ρ_{mg} is the matrix gas density in lbm/ft³; v_m is the matrix gas total velocity in md-psi/(cp-ft); ϕ_m is the matrix porosity; ρ_{scg} is the standard gas density in lbm/ft³; and V_{Esc} is the standard-condition equilibrium gas volume that is adsorbed per unit rock grain volume in scf/cf. For real-gas adsorption, many scholars used the following equation (Wu et al., 2016a; Wang et al., 2015a; Civan et al., 2013; Song et al., 2016)

$$V_{Esc} = V_L \frac{p/Z}{p/z + p_L}, \quad (26)$$

where V_L represents the Langmuir volumetric concentration in scf/cf; and p_L is the Langmuir pressure in psi. In fact, Eq. (26) (the Langmuir equation) is a function of the mean molecular speed (Langmuir, 1918). If the real-gas effects are added to the mean molecular speed, the mean molecular speed can be written as (Michel Villazon et al., 2011)

$$\bar{v} = \sqrt{\frac{8 ZRT}{\pi M}}. \quad (27)$$

In Eq. (27), we use SI units for convenience. \bar{v} is the mean molecular speed in m/s; R is the universal gas constant (8.314 J/mol/K); T is in K here; and M is the gas molar mass in kg/mol. By applying Eq. (27), the equilibrium gas volume is modified as

$$V_{Esc} = V_L \frac{p/\sqrt{Z}}{p/\sqrt{Z} + p_L}. \quad (28)$$

Eq. (28) is used to describe gas adsorption and its derivation is given

$$k_{appm} = \xi_1 \frac{\phi_m}{\tau_m} \frac{r_{pm}^2}{8} (1 + \alpha Kn) \left(1 + \frac{4Kn}{1 - bKn} \right) \left[1 + \xi_2 \frac{\mu_{mg} D_s (1 - \phi_m) p_{sc} Z T}{k_{mfg} p_m T_{sc}} \frac{V_L p_L}{2\sqrt{Z}} \frac{(1 + p_m c_{mg})}{\left(\frac{p_m}{\sqrt{Z}} + p_L \right)^2} \right], \quad (35)$$

in the Appendix. The matrix gas is produced through two mechanisms including free gas transport and adsorbed gas surface diffusion. Similar to Wasaki and Akkutlu (2015), the free gas phase and the adsorbed gas phase follow their own paths. Therefore, the total gas velocity can be expressed as the sum of the free gas velocity and adsorbed gas diffusion velocity

$$v_m = v_{mfg} + v_{ms}. \quad (29)$$

In Eq. (29), v_{mfg} is the matrix free gas velocity in md-psi/(cp-ft). Free gas transport in matrix nanopores involves the slip corrected flow and Knudsen diffusion. By using the Beskok-Karniadakis model (Beskok and

Karniadakis, 1999) to modify the permeability term, the free gas velocity can be written as

$$v_{mfg} = -\frac{k_{mfg}}{\mu_{mg}} \frac{\partial p_m}{\partial r} = -\xi_1 \frac{\phi_m}{\tau_m} \frac{r_{pm}^2}{8} (1 + \alpha Kn) \left(1 + \frac{4Kn}{1 - bKn} \right) \frac{1}{\mu_{mg}} \frac{\partial p_m}{\partial r}, \quad (30a)$$

$$k_{mfg} = k_{ml} \frac{\phi_m}{\tau_m} (1 + \alpha Kn) \left(1 + \frac{4Kn}{1 - bKn} \right), \quad (30b)$$

where k_{mfg} and k_{ml} are the matrix free gas permeability and liquid permeability of a nanopore in md; ξ_1 is a unit conversion coefficient (9.4127×10^{13} md/ft²) converting ft² into md; τ_m is the matrix tortuosity; r_{pm} is the matrix nanopore (nanochannel) radius in ft; Kn is the Knudsen number; and α and b are coefficients of the Beskok-Karniadakis model. The Knudsen number in this model is defined as $Kn = \lambda/r_{pm}$ according to Beskok and Karniadakis (1999). λ is the mean free path of gas molecules and is given by the following equation in SI units (Jennings, 1988; Michel Villazon et al., 2011)

$$\lambda = \frac{\mu_{mg}}{\rho_{ave}} \sqrt{\frac{\pi ZRT}{2M}}, \quad (31)$$

where ρ_{ave} is the average pressure in Pa. The velocity for the adsorbed gas phase is

$$v_{ms} = -\xi_2 \frac{MD_s}{\rho_{mg}} \frac{\partial C_s}{\partial r} = -\xi_2 \frac{D_s (1 - \phi_m) p_{sc} Z T}{p_m T_{sc}} \frac{V_L p_L}{2\sqrt{Z}} \frac{(1 + p_m c_{mg})}{\left(\frac{p_m}{\sqrt{Z}} + p_L \right)^2} \frac{\partial p_m}{\partial r}, \quad (32)$$

where ξ_2 is a unit conversion coefficient, 158 md-psi-D/(ft²-cp) (Ertekin et al., 1986; Zeng et al., 2017); D_s is the surface diffusion coefficient in ft²/D; T_{sc} is the standard condition temperature in K or °R; c_{mg} is the matrix gas compressibility in psi⁻¹; and C_s is matrix gas molecular concentration in lbm-mol/ft³. Here, C_s is given by

$$C_s = \frac{(1 - \phi_m) \rho_{scg} V_{Esc}}{M}. \quad (33)$$

The unit of the gas molecular weight is lbm/lbm-mol for Eq. (33). Combining Eqs. (4), (25) and (28)–(30), and (32), the mass balance equation can be written as the following pseudo-pressure form

$$\frac{1}{r^2} \frac{\partial}{\partial r} \left(r^2 k_{appmi} \frac{\partial p_{pm}}{\partial r} \right) = \mu_{mg} c_{appm} \phi_m \left(\frac{k_{appmi}}{k_{appm}} \right) \frac{\partial p_{pm}}{\partial t}, \quad (34)$$

where

$$c_{appm} = c_{mg} + \frac{p_{sc} T Z}{p_m T_{sc}} \frac{(1 - \phi_m)}{\phi_m} \frac{V_L p_L}{2\sqrt{Z}} \frac{(p_m c_{mg} + 1)}{\left(\frac{p_m}{\sqrt{Z}} + p_L \right)^2}. \quad (36)$$

Using the pseudo-pressure and pseudo-time to linearize Eq. (34) and converting it into the dimensionless form, we obtain

$$\frac{1}{r_D^2} \frac{\partial}{\partial r_D} \left(r_D^2 \frac{\partial p_{pmD}}{\partial r_D} \right) = \frac{1}{\eta_{mD}} \frac{\partial p_{pmD}}{\partial t_D}. \quad (37)$$

Correspondingly, the initial condition and boundary conditions for

Table 1
Input data for the model verification.

Parameters	Values
Reservoir size (length × width × height)	2000 ft × 1000 ft × 250 ft
Reservoir temperature	568.67 °R
Initial pressure	2300 psi
Matrix porosity	0.05
Matrix tortuosity	4.47
Water saturation	0
Matrix nanochannel (pore) radius	8×10^{-8} ft
Matrix element radius	5 ft
Langmuir volume	15.727 scf/cf
Langmuir pressure	500 psi
Total compressibility	2.5×10^{-4} psi ⁻¹
Hydraulic fracture number	4
Hydraulic fracture spacing	500 ft
Hydraulic fracture half-length	400 ft
Hydraulic fracture height	230 ft
Hydraulic fracture width	0.01 ft
Hydraulic fracture permeability (for all regions within the hydraulic fracture)	3000 md
Hydraulic fracture porosity (for all regions within the hydraulic fracture)	0.38
Secondary fracture layer thickness	1×10^{-3} ft
Secondary fracture permeability (for all regions)	200 md
Secondary fracture porosity (for all regions)	0.45
Surface diffusion coefficient	0.23 ft ² /D
Length of damaged zone 1 (no damage for this case)	20 ft
Length of the propped zone	280 ft
Length of damaged zone 2 (no damage for this case)	100 ft
Thickness of damaged zone 3 (no damage for this case)	0.01 ft
Fractal exponent (homogeneous region 1)	0
Reference permeability	2000 md
Reference height	250 ft
Reference length	250 ft
Reference porosity	0.45
Reference gas viscosity	0.0184 cp
Reference total compressibility	2.5×10^{-4} psi ⁻¹

the matrix spherical flow are shown by

$$p_{pmD}(r_D, x_D, t_D = 0) = 0, \tag{38}$$

$$p_{pmD}(r_D = 0, x_D, t_D) = p_{pmD}(0, x_D, t_D), \tag{39}$$

$$p_{pmD}(r_D = r_{mD}, x_D, t_D) = p_{pfD}(x_D, t_D). \tag{40}$$

Here, x_D represents one of the three 1-D secondary fracture flow coordinates. Because the dimensionless pseudopressure in the matrix element center is an unknown finite parameter, we define the following function to facilitate solving Eqs. (37)–(40) (Ozkan et al., 2010)

$$F_{mD}(r_D, x_D, t_D) = r_D p_{pmD}(r_D, x_D, t_D). \tag{41}$$

Therefore, in the Laplace domain, Eqs. (37) and (39) and (40) can be written as

$$\frac{\partial^2 \bar{F}_{mD}}{\partial r_D^2} - \frac{s}{\eta_{mD}} \bar{F}_{mD} = 0, \tag{42}$$

$$\bar{F}_{mD}(r_D = 0, x_D, s) = 0, \tag{43}$$

$$\bar{F}_{mD}(r_{mD}, x_D, s) = r_{mD} \bar{p}_{pfD}(x_D, s). \tag{44}$$

Solving Eqs. (42)–(44) gives

$$\bar{F}_{mD}(r_D, x_D, s) = \frac{r_{mD} \sinh(\sqrt{s/\eta_{mD}} r_D)}{\sinh(\sqrt{s/\eta_{mD}} r_{mD})} \bar{p}_{pfD}(x_D, s). \tag{45}$$

Therefore, the solution for the matrix flow is obtained

$$p_{pmD}(r_D, x_D, s) = \frac{r_{mD} \sinh(\sqrt{s/\eta_{mD}} r_D)}{r_D \sinh(\sqrt{s/\eta_{mD}} r_{mD})} \bar{p}_{pfD}(x_D, s). \tag{46}$$

3.2. USRV flow models

The matrix gas is instantaneously and uniformly distributed in the 1/2 volume of the secondary fracture layer. Therefore, mass transfer between the matrix and the secondary fracture layer can be written as (Ozkan et al., 2010; Zeng et al., 2017)

$$f(x, t) = - \frac{2}{h_f} \left(\rho_{mg} \frac{k_{appmi}}{\mu_{mg}} \frac{\partial p_m}{\partial r} \right) \Big|_{(r_m, x, t)}. \tag{47}$$

Then, the mass balance equation for the secondary fracture linear flow in USRVs is

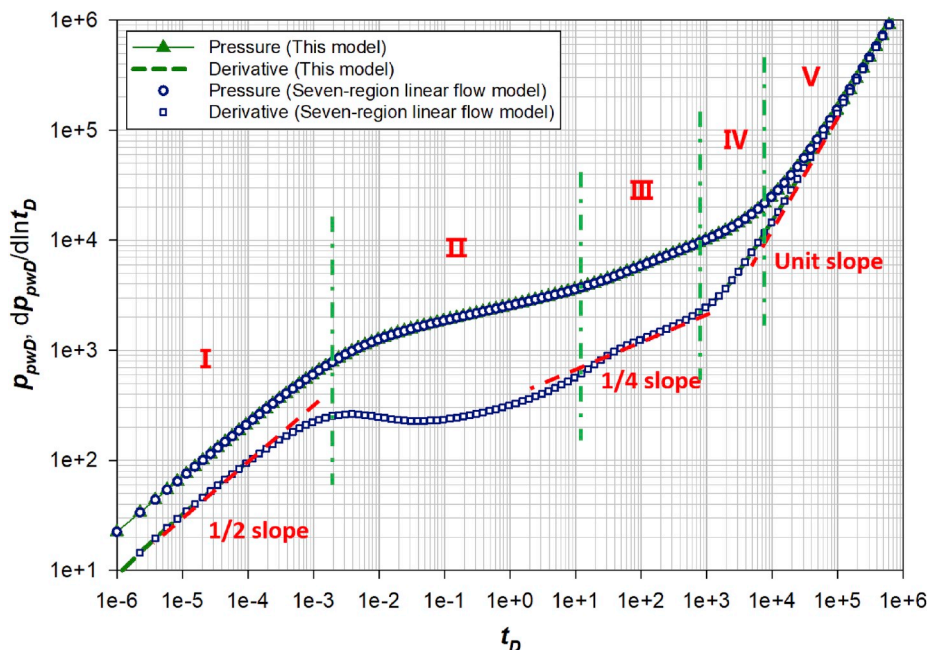


Fig. 6. Comparison between the seven-region linear flow model (Zeng et al., 2017) and the degraded model.

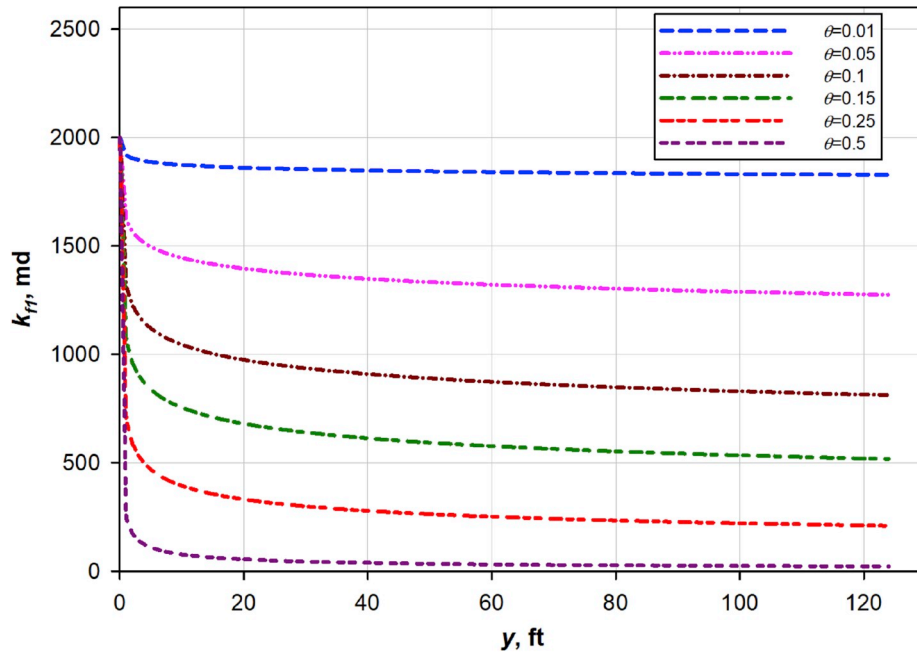


Fig. 7. Secondary fracture permeability variation along the y-direction in the SRVs with different SRV fractal exponents.

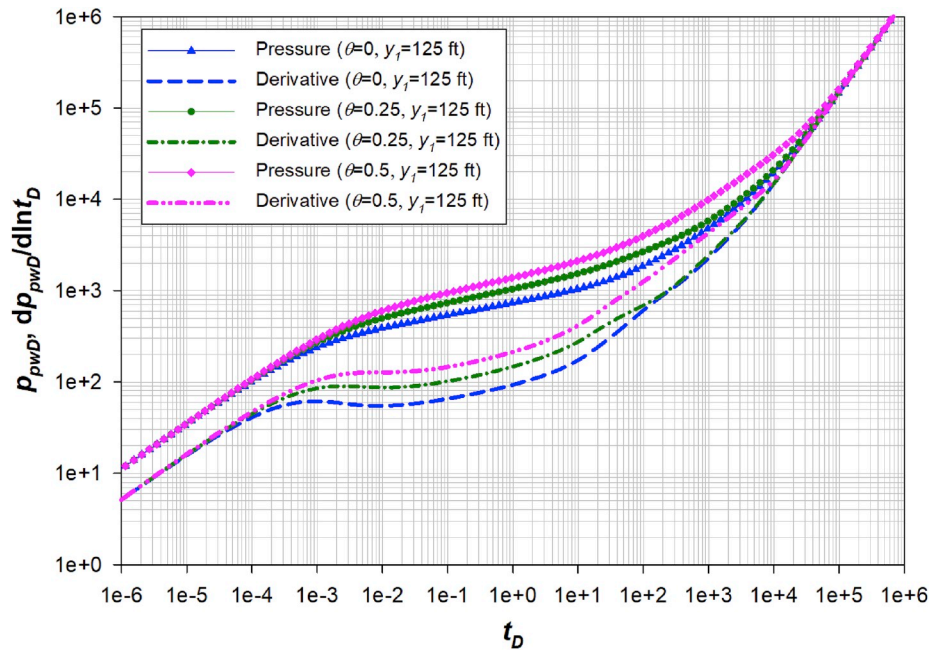


Fig. 8. Effects of the SRV fractal exponent on pressure responses.

$$-\frac{\partial(\rho_{fg} v_f)}{\partial x} + \left[-\frac{2}{h_f} \left(\rho_{mg} \frac{k_{appm}}{\mu_{mg}} \frac{\partial p_m}{\partial r} \right) \Big|_{(r_m, x, t)} \right] = \frac{\partial(\rho_{fg} \phi_f)}{\partial t}. \quad (48)$$

Rewriting the above equation in the dimensionless pseudopressure form in the Laplace domain, we obtain the diffusivity equation that couples the matrix flow and the secondary fracture flow as follow

$$\frac{\partial^2 \bar{p}_{pD}}{\partial x_D^2} - c(s) \bar{p}_{pD} = 0, \quad (49)$$

where the c -function is

$$c(s) = \frac{s}{\eta_{fD}} - \frac{2k_{appm} d_{ref}}{h_f k_f} \left[\frac{1}{r_{mD}} - \sqrt{\frac{s}{\eta_{mD}}} \coth \left(\sqrt{\frac{s}{\eta_{mD}}} r_{mD} \right) \right]. \quad (50)$$

3.2.1. Region 6

For region 6, the 1-D diffusivity equation can be written as

$$\frac{\partial^2 \bar{p}_{pD6}}{\partial x_D^2} - c(s) \bar{p}_{pD6} = 0. \quad (51)$$

The no-flow boundary condition at the top or bottom of the reservoir is

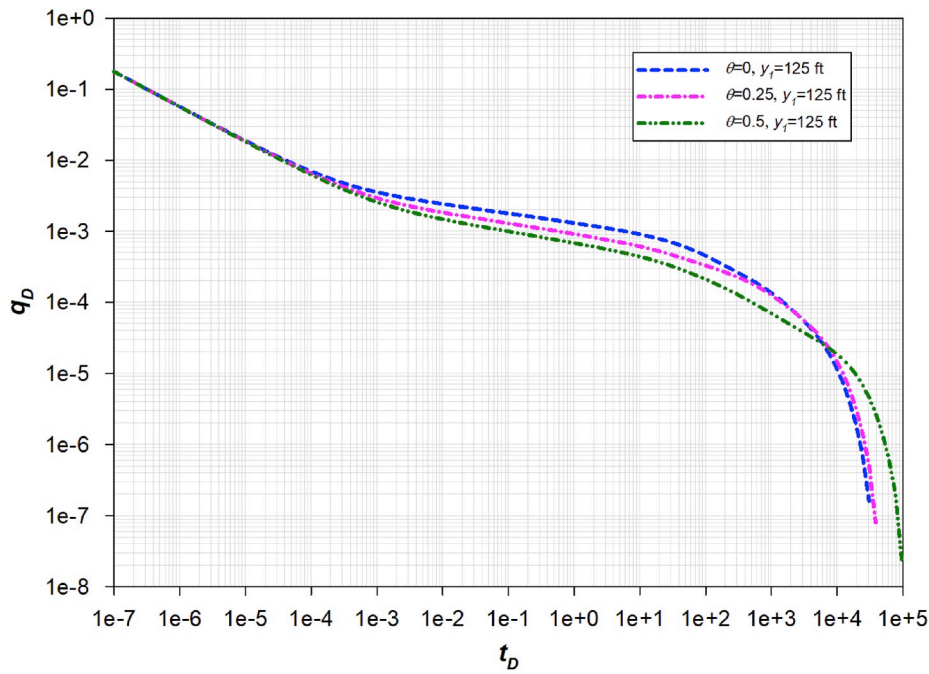


Fig. 9. Effects of the SRV fractal exponent on rate responses.

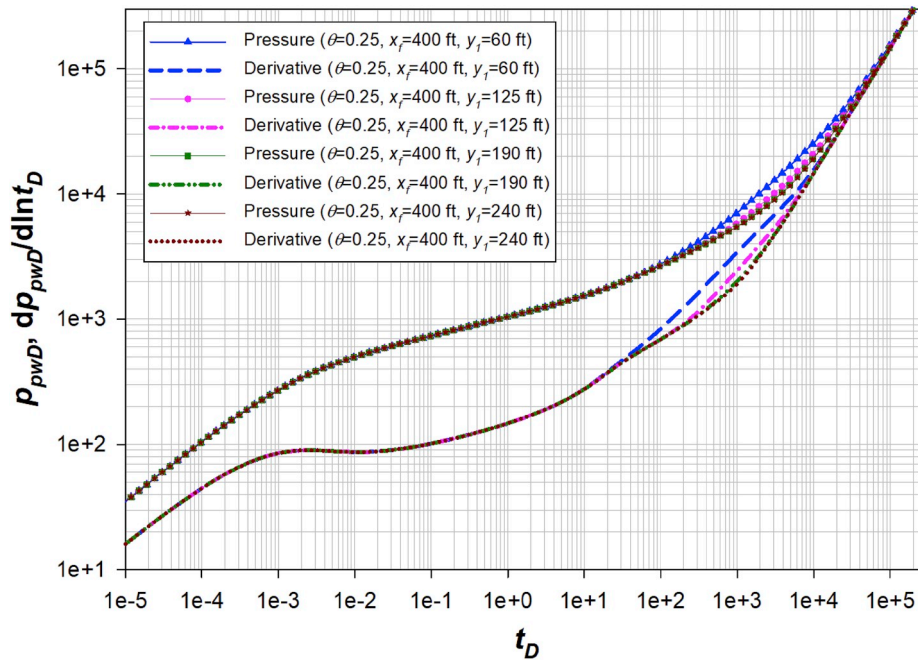


Fig. 10. Effects of the SRV width on pressure responses.

$$\left. \frac{\partial \bar{p}_{p/D6}}{\partial z_D} \right|_{z_D=z_{2D}} = 0. \tag{52}$$

And the pressure continuity conditions on the interfaces of regions 6 and 2 and regions 6 and 4 are given by

$$\bar{p}_{p/D6} \Big|_{z_D=z_{1D}} = \bar{p}_{p/D2} \Big|_{z_D=z_{1D}} = \bar{p}_{p/D4} \Big|_{z_D=z_{1D}}. \tag{53}$$

Solving Eqs. (51)–(53) gives the solutions of region 6

$$\left. \frac{\partial \bar{p}_{p/D6}}{\partial z_D} \right|_{z_D=z_{1D}} = -\bar{p}_{p/D2} \Big|_{z_D=z_{1D}} \sqrt{c(s)_6} \tanh[\sqrt{c(s)_6} (z_{2D} - z_{1D})], \tag{54a}$$

$$\left. \frac{\partial \bar{p}_{p/D6}}{\partial z_D} \right|_{z_D=z_{1D}} = -\bar{p}_{p/D4} \Big|_{z_D=z_{1D}} \sqrt{c(s)_6} \tanh[\sqrt{c(s)_6} (z_{2D} - z_{1D})]. \tag{54b}$$

3.2.2. Region 5

Similarly, for region 5, the 1-D diffusivity equation can be written as

$$\frac{\partial^2 \bar{p}_{p/D5}}{\partial z_D^2} - c(s)_5 \bar{p}_{p/D5} = 0. \tag{55}$$

The no-flow boundary condition at $z_D = z_{2D}$ is

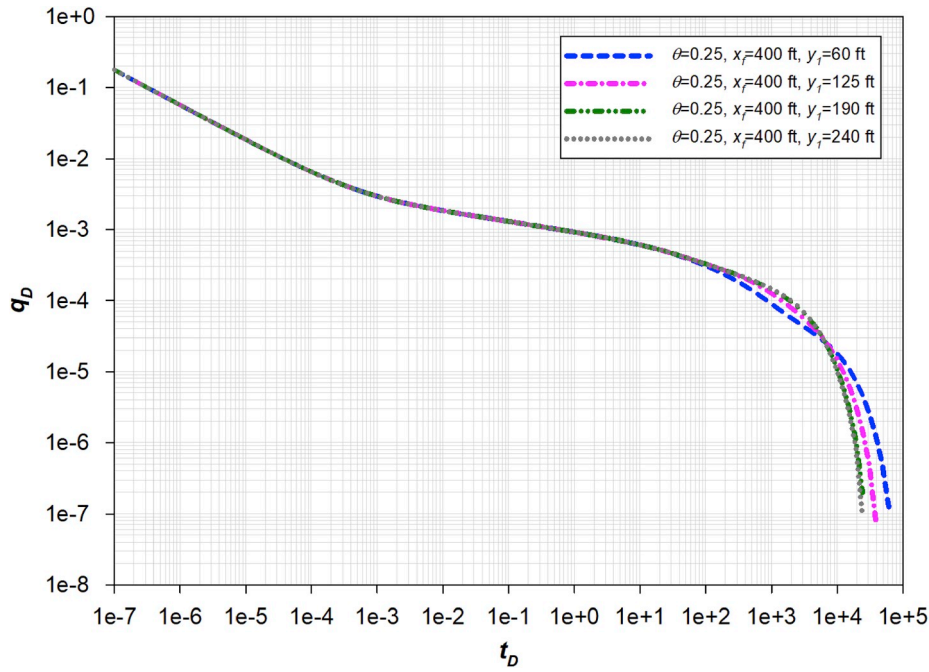


Fig. 11. Effects of the SRV width on rate responses.

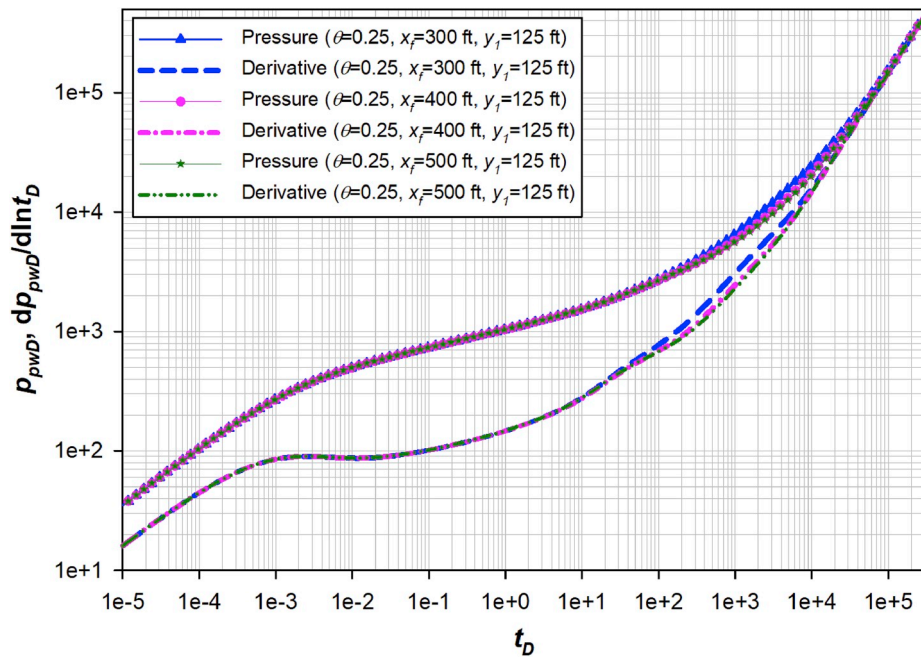


Fig. 12. Effects of the SRV length on pressure responses.

$$\frac{\partial \bar{p}_{p/D5}}{\partial z_D} \Big|_{z_D=z_{2D}} = 0. \tag{56}$$

And the pressure continuity conditions on the interfaces of regions 5 and 1, regions 5 and 3, and region 5 and damaged zone 3 are

$$\bar{p}_{p/D5} \Big|_{z_D=z_{1D}} = \bar{p}_{p/D1} \Big|_{z_D=z_{1D}} = \bar{p}_{p/D3} \Big|_{z_D=z_{1D}} = \bar{p}_{p/Ds} \Big|_{z_D=z_{1D}}. \tag{57}$$

Solving Eqs. (55)–(57), we obtain the solutions of region 5

$$\frac{\partial \bar{p}_{p/D5}}{\partial z_D} \Big|_{z_D=z_{1D}} = -\bar{p}_{p/D1} \Big|_{z_D=z_{1D}} \sqrt{c(s)}_5 \tanh[\sqrt{c(s)}_5 (z_{2D} - z_{1D})], \tag{58a}$$

$$\frac{\partial \bar{p}_{p/D5}}{\partial z_D} \Big|_{z_D=z_{1D}} = -\bar{p}_{p/D3} \Big|_{z_D=z_{1D}} \sqrt{c(s)}_5 \tanh[\sqrt{c(s)}_5 (z_{2D} - z_{1D})], \tag{58b}$$

$$\frac{\partial \bar{p}_{p/D5}}{\partial z_D} \Big|_{z_D=z_{1D}} = -\bar{p}_{p/Ds} \Big|_{z_D=z_{1D}} \sqrt{c(s)}_5 \tanh[\sqrt{c(s)}_5 (z_{2D} - z_{1D})]. \tag{58c}$$

3.2.3. Region 4

For region 4, the diffusivity equation is given by

$$\frac{\partial^2 \bar{p}_{p/D4}}{\partial x_D^2} + \frac{k_{f6}}{k_{f4} z_{1D}} \frac{\partial \bar{p}_{p/D6}}{\partial z_D} \Big|_{z_D=z_{1D}} - c(s)_4 \bar{p}_{p/D4} = 0. \tag{59}$$

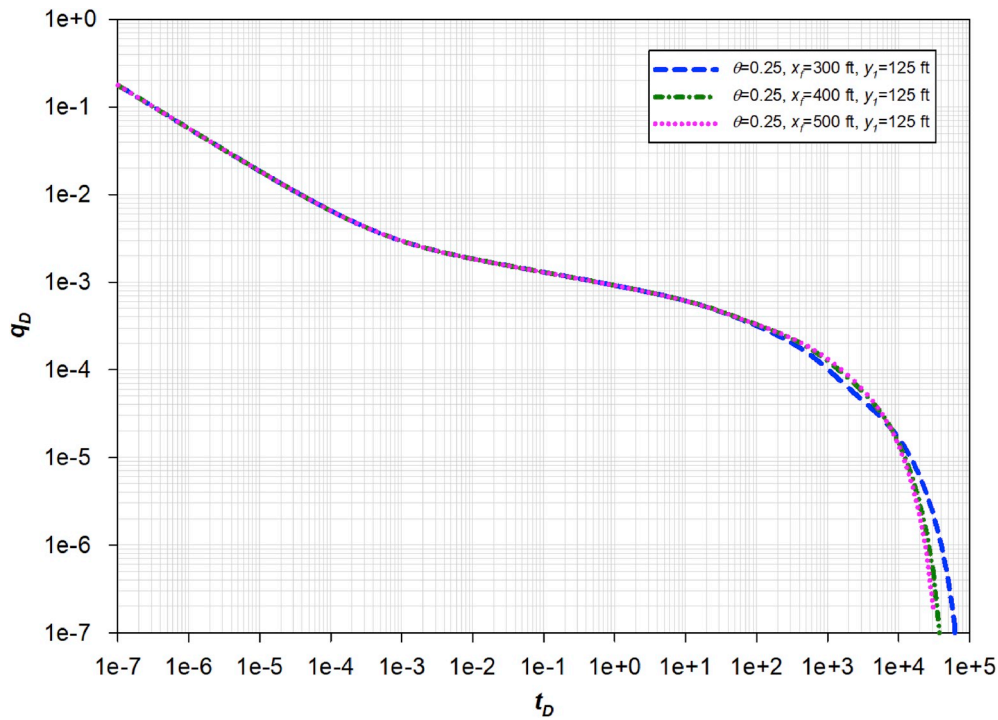


Fig. 13. Effects of the SRV length on rate responses.

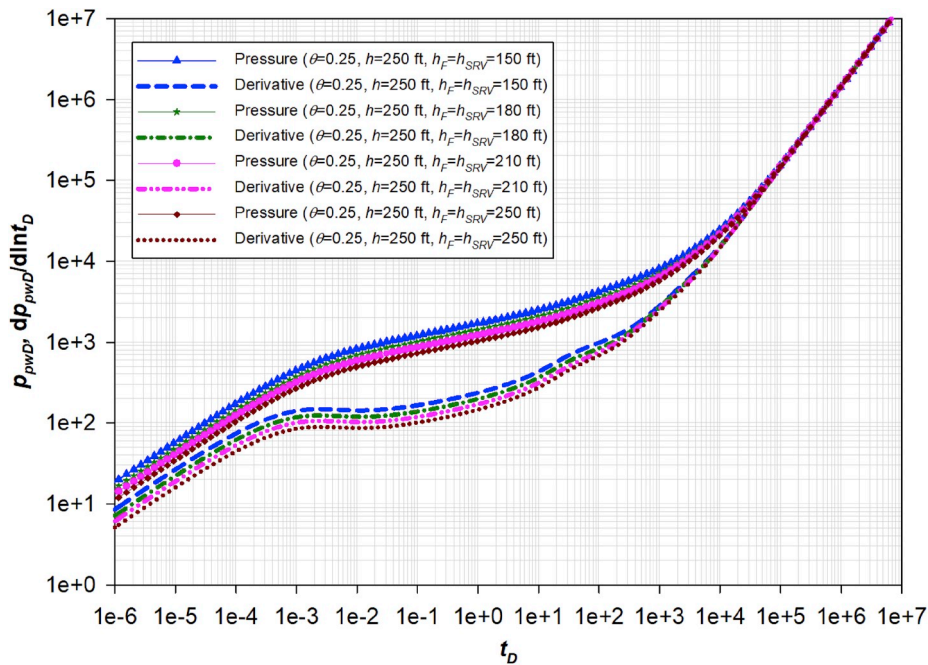


Fig. 14. Effects of the SRV height on pressure responses.

The no-flow condition at the reservoir outer boundary is

$$\left. \frac{\partial \bar{p}_{pfd4}}{\partial x_D} \right|_{x_D=x_{eD}} = 0. \tag{60}$$

And the pressure continuity condition at $x_D = x_{1D}$ between regions 4 and 2 can be written as

$$\bar{p}_{pfd4} \Big|_{x_D=x_{1D}} = \bar{p}_{pfd2} \Big|_{x_D=x_{1D}}. \tag{61}$$

Solving Eqs. (59)–(61) gives the solution of region 4

$$\left. \frac{\partial \bar{p}_{pfd4}}{\partial x_D} \right|_{x_D=x_{1D}} = -\bar{p}_{pfd2} \Big|_{x_D=x_{1D}} \sqrt{\alpha_4} \tanh \left[\sqrt{\alpha_4} (x_{eD} - x_{1D}) \right], \tag{62}$$

where

$$\alpha_4 = \frac{k_{f6}}{k_{f4} z_{1D}} \sqrt{c(s)_6} \tanh \left[\sqrt{c(s)_6} (z_{2D} - z_{1D}) \right] + c(s)_4. \tag{63}$$

3.2.4. Region 3

Similarly, we have the diffusivity equation for region 3 as follow

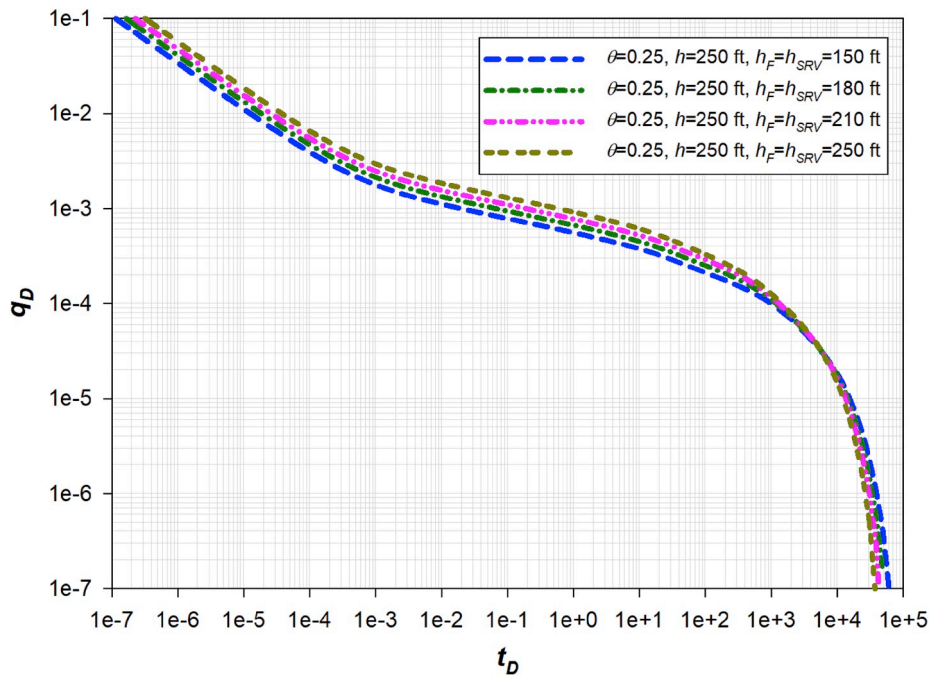


Fig. 15. Effects of the SRV height on rate responses.

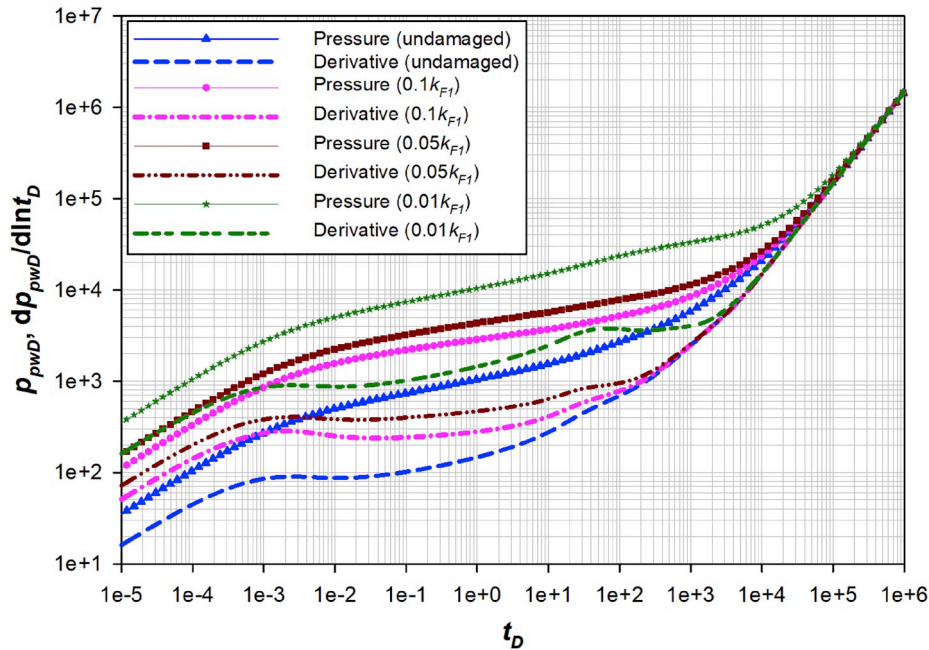


Fig. 16. Effects of choked fractures on pressure responses.

$$\frac{\partial^2 \bar{p}_{pFD3}}{\partial x_D^2} + \frac{k_{f5}}{k_{f3}z_{1D}} \frac{\partial \bar{p}_{pFD5}}{\partial z_D} \Big|_{z_D=z_{1D}} - c(s)_3 \bar{p}_{pFD3} = 0. \quad (64)$$

The no-flow condition at the reservoir outer boundary is

$$\frac{\partial \bar{p}_{pFD3}}{\partial x_D} \Big|_{x_D=x_eD} = 0. \quad (65)$$

And the pressure continuity conditions between regions 3 and 1, and region 3 and damaged zone 3 are

$$\bar{p}_{pFD3} \Big|_{x_D=x_{1D}} = \bar{p}_{pFD1} \Big|_{x_D=x_{1D}} = \bar{p}_{pFD8} \Big|_{x_D=x_{1D}}. \quad (66)$$

Solving Eqs. (64)–(66) gives the solutions for region 3

$$\frac{\partial \bar{p}_{pFD3}}{\partial x_D} \Big|_{x_D=x_{1D}} = -\bar{p}_{pFD1} \Big|_{x_D=x_{1D}} \sqrt{\alpha_3} \tanh \left[\sqrt{\alpha_3} (x_{eD} - x_{1D}) \right], \quad (67a)$$

$$\frac{\partial \bar{p}_{pFD3}}{\partial x_D} \Big|_{x_D=x_{1D}} = -\bar{p}_{pFD8} \Big|_{x_D=x_{1D}} \sqrt{\alpha_3} \tanh \left[\sqrt{\alpha_3} (x_{eD} - x_{1D}) \right], \quad (67b)$$

where

$$\alpha_3 = \frac{k_{f5}}{k_{f3}z_{1D}} \sqrt{c(s)_5} \tanh \left[\sqrt{c(s)_5} (z_{2D} - z_{1D}) \right] + c(s)_3. \quad (68)$$

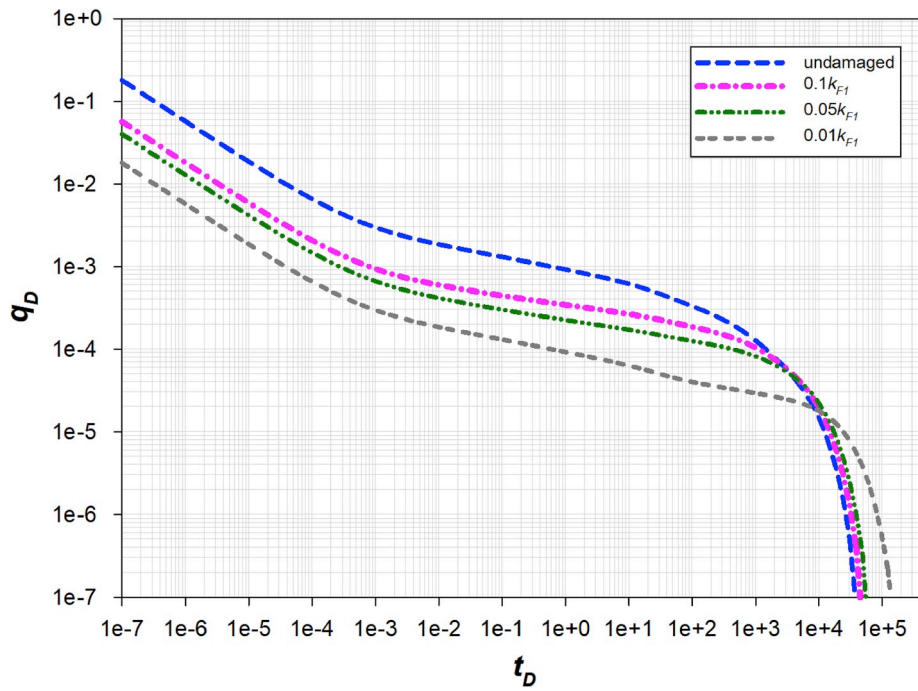


Fig. 17. Effects of choked fractures on rate responses.

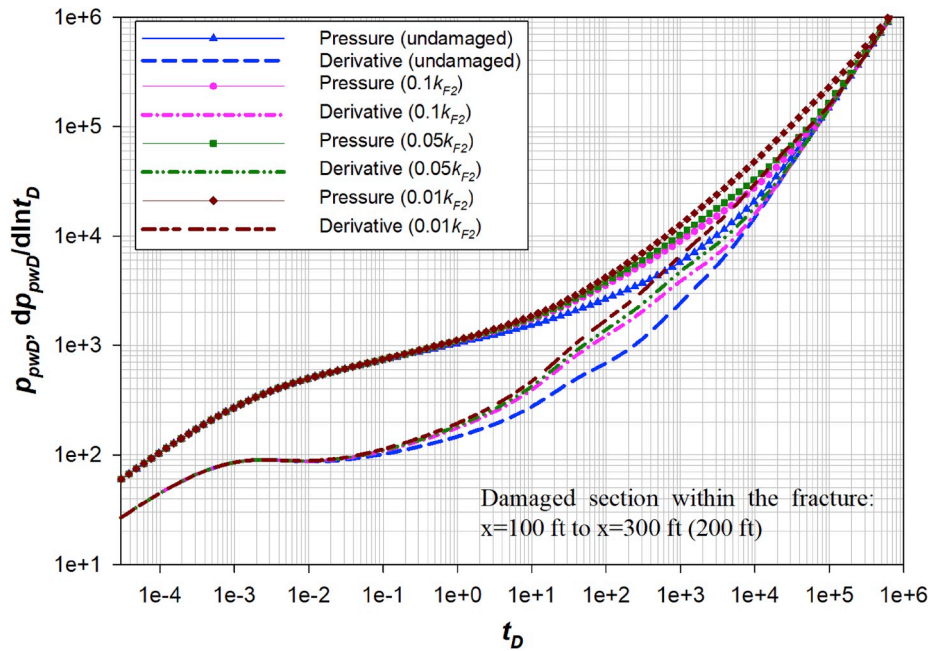


Fig. 18. Effects of the damaged middle section on pressure responses.

3.2.5. Region 2

For region 2, the diffusivity equation is given by

$$\frac{\partial^2 \bar{p}_{pD2}}{\partial y_D^2} + \frac{k_{f6}}{k_{f2}z_{1D}} \frac{\partial \bar{p}_{pD6}}{\partial z_D} \Big|_{z_D=z_{1D}} + \frac{k_{f4}}{k_{f2}x_{1D}} \frac{\partial \bar{p}_{pD4}}{\partial x_D} \Big|_{x_D=x_{1D}} - c(s)_2 \bar{p}_{pD2} = 0. \quad (69)$$

The no-flow boundary condition between two adjacent hydraulic fractures is shown by

$$\frac{\partial \bar{p}_{pD2}}{\partial y_D} \Big|_{y_D=y_{2D}} = 0. \quad (70)$$

And the pressure continuity condition between regions 2 and 1 is

$$\bar{p}_{pD2} \Big|_{y_D=y_{1D}} = \bar{p}_{pD1} \Big|_{y_D=y_{1D}}. \quad (71)$$

Solving Eqs. (69)–(71) gives the solution of region 2

$$\frac{\partial \bar{p}_{pD2}}{\partial y_D} \Big|_{y_D=y_{1D}} = -\bar{p}_{pD1} \Big|_{y_D=y_{1D}} \sqrt{\alpha_2} \tanh \left[\sqrt{\alpha_2} (y_{2D} - y_{1D}) \right], \quad (72)$$

where

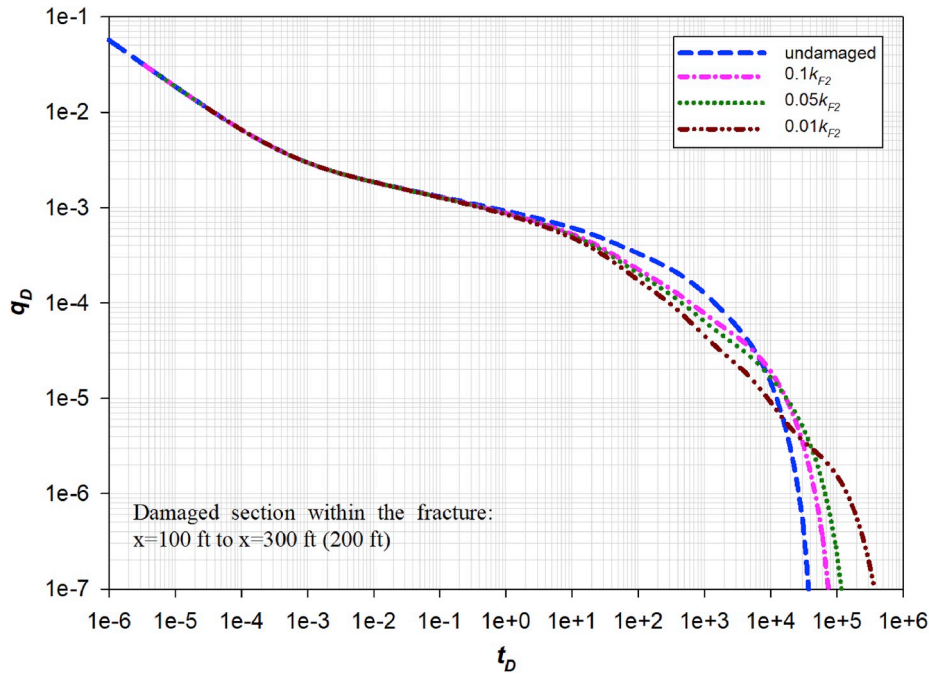


Fig. 19. Effects of the damaged middle section on rate responses.

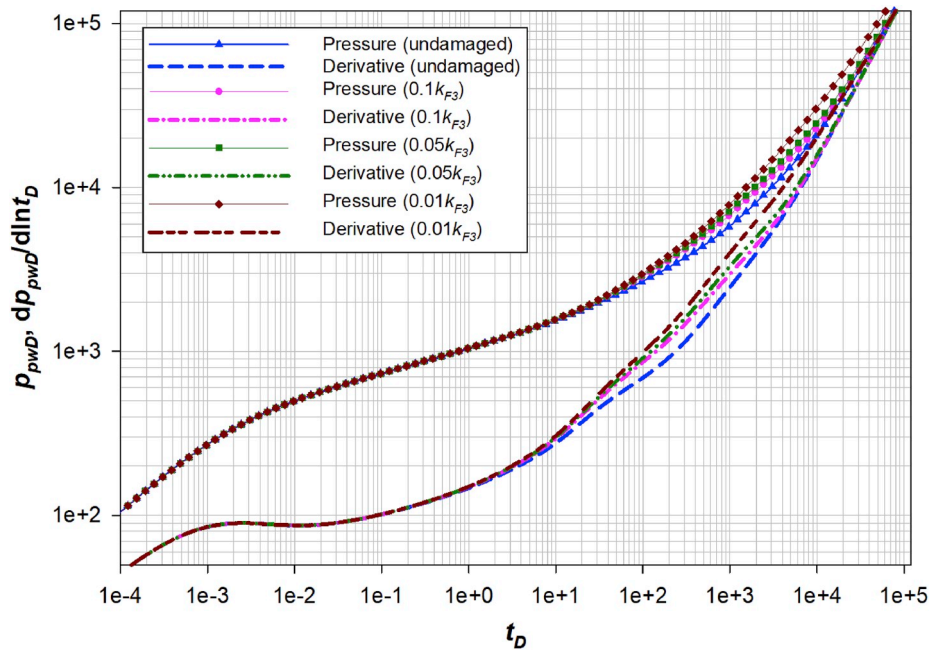


Fig. 20. Effects of the damaged section near the fracture tip on pressure responses.

$$\alpha_2 = \frac{k_{f6}}{k_{f2}z_{1D}} \sqrt{c(s)}_6 \tanh[\sqrt{c(s)}_6 (z_{2D} - z_{1D})] + \frac{k_{f4}}{k_{f2}x_{1D}} \sqrt{\alpha_4} \tanh[\sqrt{\alpha_4} (x_{eD} - x_{1D})] + c(s)_2. \quad (73)$$

Now all the solutions for USRVs are obtained.

3.3. SRV flow models

The mass balance equation for the secondary fracture linear flow in

SRVs is given by

$$\frac{\partial \left[k_{JSRV}(y) \frac{\partial p_{pf}}{\partial y} \right]}{\partial y} + k_{JSRV}(y) \frac{\partial^2 p_{pf}}{\partial x^2} + k_{JSRV}(y) \frac{\partial^2 p_{pf}}{\partial z^2} + \left[\left(-\frac{2k_{appmi}}{h_f} \frac{\partial p_{pm}}{\partial r} \right) \Big|_{(r_m-x,t)} \right] = \phi_{JSRV}(y) c_{fg} \mu_{fg} \frac{\partial p_{pf}}{\partial t}. \quad (74)$$

Converting Eq. (74) into the dimensionless form in the Laplace domain yields

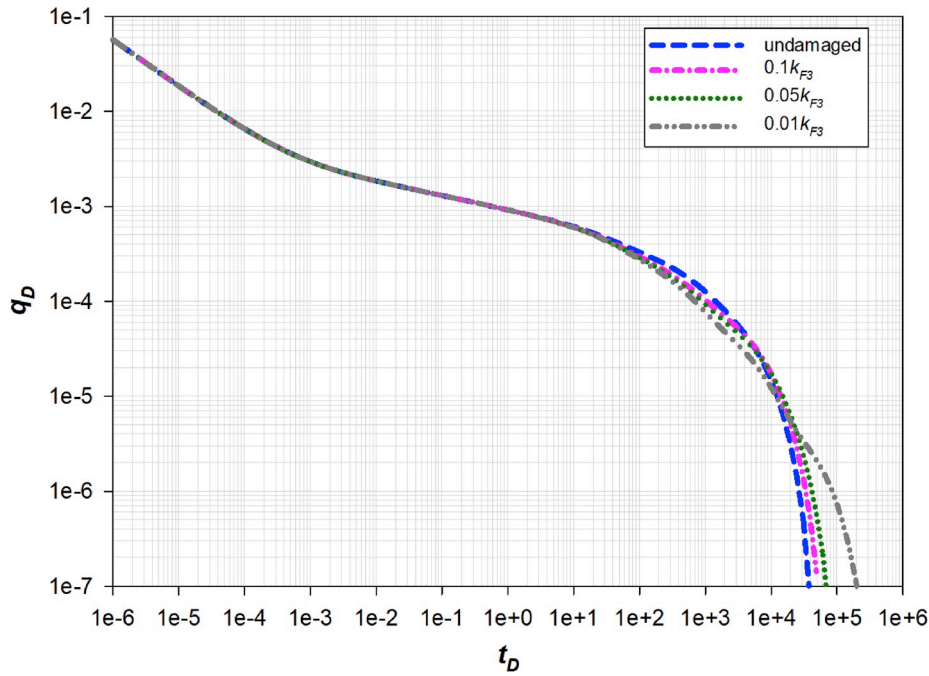


Fig. 21. Effects of the damaged section near the fracture tip on rate responses.

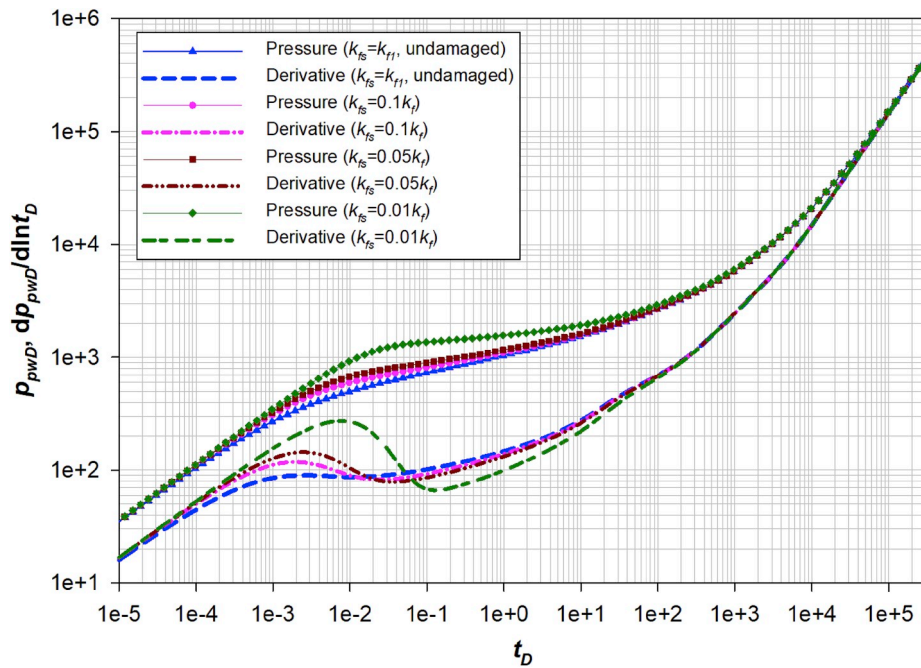


Fig. 22. Effects of fracture face damage on pressure responses.

$$\frac{\partial^2 \bar{p}_{pD1}}{\partial y_D^2} - \frac{\theta}{y_D} \frac{\partial \bar{p}_{pD1}}{\partial y_D} + \frac{k_{f3}}{k_{f1} x_{1D}} \left(\frac{y_D}{y_{sD}} \right)^\theta \frac{\partial \bar{p}_{pD3}}{\partial x_D} \Big|_{x_{1D}} + \frac{k_{f5}}{k_{f1} z_{1D}} \left(\frac{y_D}{y_{sD}} \right)^\theta \frac{\partial \bar{p}_{pD5}}{\partial z_D} \Big|_{z_{1D}} - c(s)_1 \left(\frac{y_D}{y_{sD}} \right)^\theta \bar{p}_{pD1} = 0. \quad (75)$$

The above equation can be rewritten as

$$\frac{\partial^2 \bar{p}_{pD1}}{\partial y_D^2} - \frac{\theta}{y_D} \frac{\partial \bar{p}_{pD1}}{\partial y_D} - \alpha_1 \left(\frac{y_D}{y_{sD}} \right)^\theta \bar{p}_{pD1} = 0, \quad (76)$$

where

$$\alpha_1 = \left\{ c(s)_1 + \frac{k_{f3}}{k_{f1} x_{1D}} \sqrt{\alpha_3} \tanh \left[\sqrt{\alpha_3} (x_{eD} - x_{1D}) \right] + \frac{k_{f5}}{k_{f1} z_{1D}} \sqrt{c(s)_5} \tanh \left[\sqrt{c(s)_5} (z_{2D} - z_{1D}) \right] \right\}. \quad (77)$$

Eq. (76) is the diffusivity equation for the SRV (region 1). The flux continuity condition between regions 1 and 2 is

$$\frac{\partial \bar{p}_{pD1}}{\partial y_D} \Big|_{y_D=y_{1D}} = \frac{k_{f2}}{k_{f1}} \left(\frac{y_{1D}}{y_{sD}} \right)^\theta \frac{\partial \bar{p}_{pD2}}{\partial y_D} \Big|_{y_D=y_{1D}}. \quad (78)$$

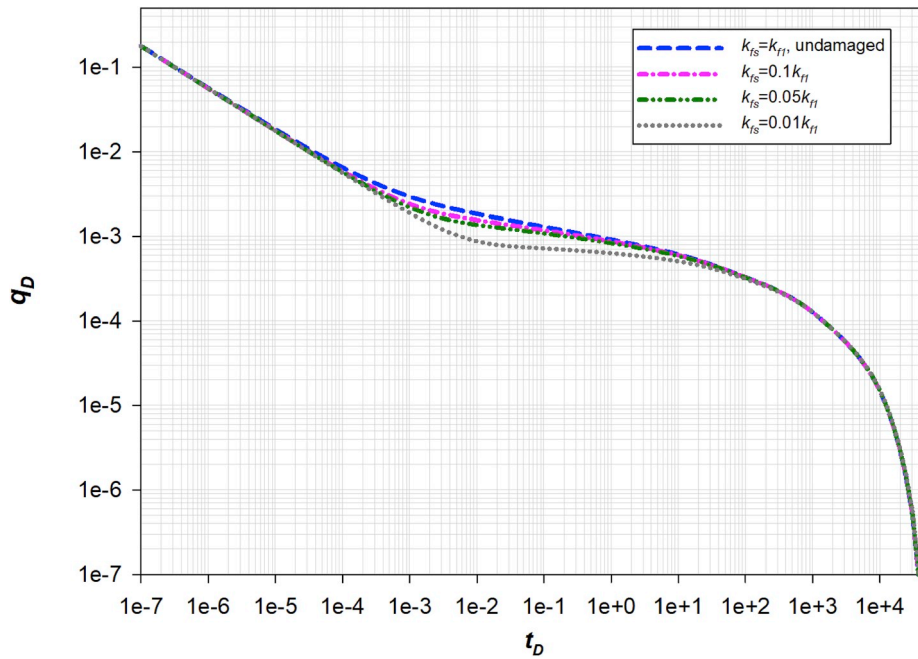


Fig. 23. Effects of fracture face damage on rate responses.

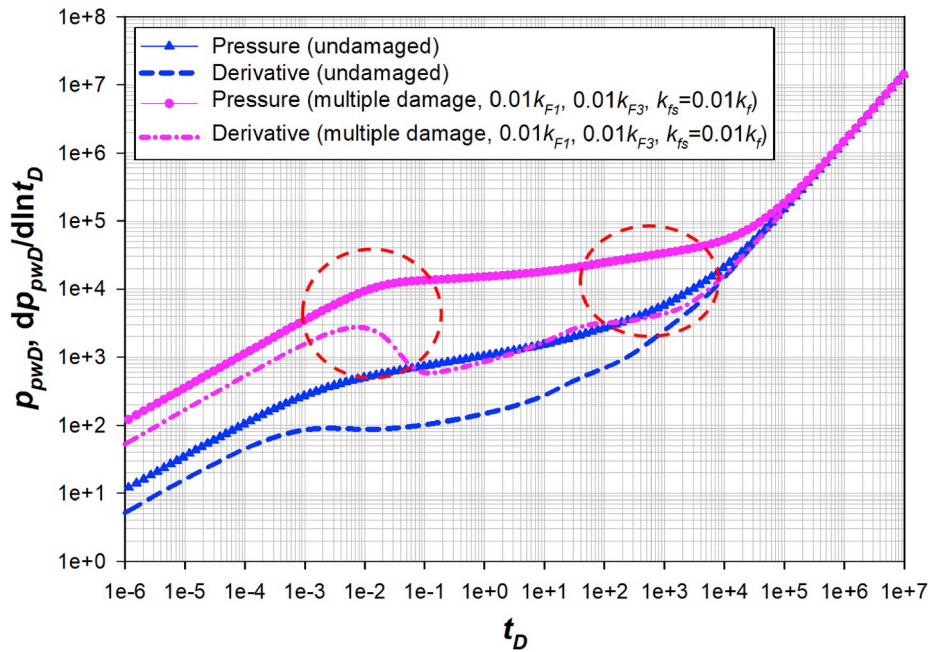


Fig. 24. Effects of multiple fracture damage on pressure responses.

And the pressure continuity condition between region 1 and damaged zone 3 is

$$\bar{p}_{pD1} \Big|_{y_D=y_{sD}} = \bar{p}_{pDs} \Big|_{y_D=y_{sD}} \tag{79}$$

Solving Eqs. (76)-(79) through the method of Fan and Etehadta-vakkol (2017a), we obtain the solution for the SRV

$$\frac{\partial \bar{p}_{pD1}}{\partial y_D} \Big|_{y_D=y_{sD}} = \bar{p}_{pDs} \Big|_{y_D=y_{sD}} \beta_1, \tag{80}$$

where

$$\beta_1 = \frac{\lambda_1 \omega (y_{sD})^{\omega-1} \{ I_{\nu-1} [\lambda_1 (y_{sD})^\omega] \sigma - K_{\nu-1} [\lambda_1 (y_{sD})^\omega] \}}{I_\nu [\lambda_1 (y_{sD})^\omega] \sigma + K_\nu [\lambda_1 (y_{sD})^\omega]} \tag{81}$$

$$\lambda_1 = \frac{\sqrt{\alpha_1 (y_{sD})^{-\theta}}}{\omega}, \tag{82}$$

$$\omega = \frac{\theta + 2}{2}, \tag{83}$$

$$\gamma = \frac{\theta + 1}{2}, \tag{84}$$

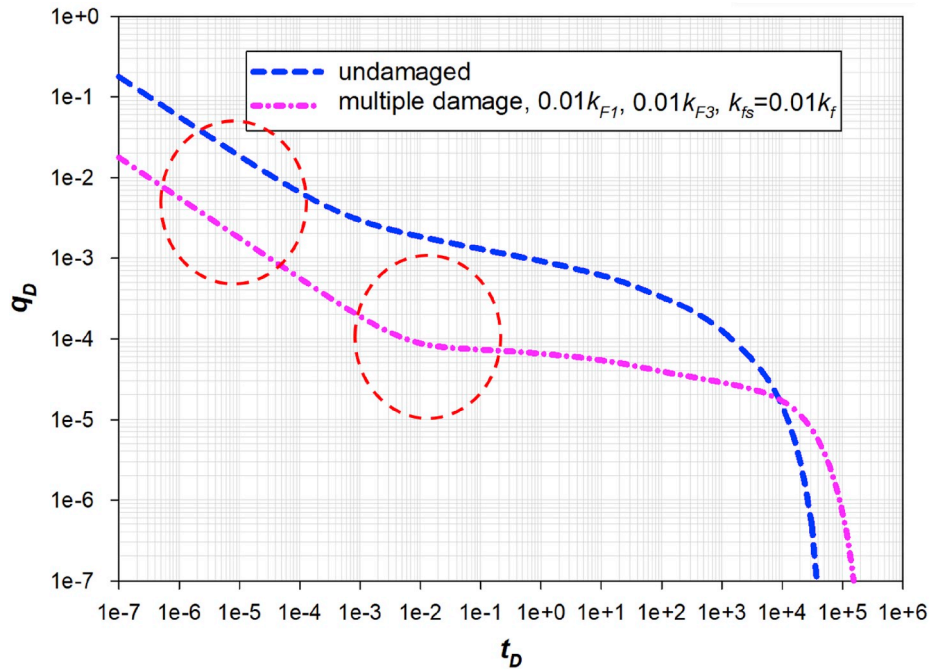


Fig. 25. Effects of multiple fracture damage on rate responses.

$$\sigma = \frac{\lambda_1 \omega y_{1D}^{\omega-1} K_{\nu-1}(\lambda_1 y_{1D}^{\omega}) - \frac{k_{f2}}{k_{f1}} \left(\frac{y_{1D}}{y_{sD}}\right)^{\theta} \sqrt{\alpha_2} \tanh[\sqrt{\alpha_2}(y_{2D} - y_{1D})] K_{\nu}(\lambda_1 y_{1D}^{\omega})}{\lambda_1 \omega y_{1D}^{\omega-1} I_{\nu-1}(\lambda_1 y_{1D}^{\omega}) + \frac{k_{f2}}{k_{f1}} \left(\frac{y_{1D}}{y_{sD}}\right)^{\theta} \sqrt{\alpha_2} \tanh[\sqrt{\alpha_2}(y_{2D} - y_{1D})] I_{\nu}(\lambda_1 y_{1D}^{\omega})} \quad (85)$$

$I_{\nu}(x)$ and $K_{\nu}(x)$ are the two linearly independent solutions of the modified Bessel's equation. And ν is the order.

3.4. Fracture sub-region flow models

3.4.1. Damaged zone 3

For damaged zone 3, the diffusivity equation is shown by

$$\frac{\partial^2 \bar{p}_{pFD3}}{\partial y_D^2} + \frac{k_{f3}}{k_{fs} x_{1D}} \frac{\partial \bar{p}_{pFD3}}{\partial x_D} \Big|_{x_D=x_{1D}} + \frac{k_{f5}}{k_{fs} z_{1D}} \frac{\partial \bar{p}_{pFD3}}{\partial z_D} \Big|_{z_D=z_{1D}} - c(s)_s \bar{p}_{pFD3} = 0. \quad (86)$$

where k_{fs} is the secondary fracture permeability of damaged zone 3 in md. In damaged zone 3, secondary fracture permeability is lower compared with that of USRVs. The flux continuity condition between

region 1 and damaged zone 3 is

$$k_{f1} \left(\frac{y_{sD}}{y_{sD}}\right)^{-\theta} \frac{\partial \bar{p}_{pFD1}}{\partial y_D} \Big|_{y_D=y_{sD}} = k_{fs} \frac{\partial \bar{p}_{pFD3}}{\partial y_D} \Big|_{y_D=y_{sD}}. \quad (87)$$

The pressure continuity conditions between damaged zone 3 and the primary hydraulic fracture are

$$\bar{p}_{pFD3} \Big|_{y_D=\frac{w_D}{2}} = \bar{p}_{pFD1} \Big|_{y_D=\frac{w_D}{2}} = \bar{p}_{pFD2} \Big|_{y_D=\frac{w_D}{2}} = \bar{p}_{pFD3} \Big|_{y_D=\frac{w_D}{2}}, \quad (88)$$

Solving Eqs. (86)-(88) gives the solution of damaged zone 3

$$\frac{\partial \bar{p}_{pFD3}}{\partial y_D} \Big|_{y_D=\frac{w_D}{2}} = \beta_2 \bar{p}_{pFD1} \Big|_{y_D=\frac{w_D}{2}} = \beta_2 \bar{p}_{pFD2} \Big|_{y_D=\frac{w_D}{2}} = \beta_2 \bar{p}_{pFD3} \Big|_{y_D=\frac{w_D}{2}}, \quad (89)$$

where

$$\beta_2 = \sqrt{\alpha_s} \frac{\left(k_{fs} \sqrt{\alpha_s} + k_{f1} \beta_1\right) \exp\left[\sqrt{\alpha_s} \left(\frac{w_D}{2} - y_{sD}\right)\right] - \left(k_{fs} \sqrt{\alpha_s} - k_{f1} \beta_1\right) \exp\left[-\sqrt{\alpha_s} \left(\frac{w_D}{2} - y_{sD}\right)\right]}{\left(k_{fs} \sqrt{\alpha_s} + k_{f1} \beta_1\right) \exp\left[\sqrt{\alpha_s} \left(\frac{w_D}{2} - y_{sD}\right)\right] + \left(k_{fs} \sqrt{\alpha_s} - k_{f1} \beta_1\right) \exp\left[-\sqrt{\alpha_s} \left(\frac{w_D}{2} - y_{sD}\right)\right]}, \quad (90)$$

Table 2
Reservoir and MFHW properties for matching the Marcellus well performance.

Parameters	Values
Reservoir size (length × width × height)	5000 ft × 1400 ft × 100 ft
Reservoir temperature	609.67 °R
Initial pressure	5300 psi
Bottom-hole pressure	1000 psi
Effective matrix porosity	0.0608
Matrix tortuosity	4.05
Water saturation	0.24
Matrix nanotube (pore) radius	2.3×10^{-8} ft
Matrix element radius	5 ft
Langmuir volume	15.727 scf/cf
Langmuir pressure	500 psi
Total compressibility	2.28×10^{-4} psi ⁻¹
Hydraulic fracture number	10
Hydraulic fracture spacing	500 ft
Hydraulic fracture half-length	520 ft
SRV half-width	125 ft
Hydraulic fracture height	100 ft
Hydraulic fracture width	0.01 ft
Hydraulic fracture permeability (damaged zone 1)	8 md
Hydraulic fracture permeability (propped zone)	1000 md
Hydraulic fracture permeability (damaged zone 3, no damage)	1000 md
Hydraulic fracture porosity (for all regions within the hydraulic fracture)	0.38
Secondary fracture layer thickness (for all regions)	1×10^{-3} ft
Secondary fracture permeability (USRVs)	30 md
Secondary fracture permeability (damaged zone 3)	0.3 md
Maximal secondary fracture permeability (SRVs)	400 md
Secondary fracture porosity (for all regions)	0.45
Surface diffusion coefficient	0.23 ft ² /D
Length of damaged zone 1	33 ft
Length of the propped zone	267 ft
Length of damaged zone 2 (no damage here)	220 ft
Thickness of damaged zone 3 (no damage for this case)	0.01 ft
Fractal exponent	0.25
Reference permeability	2000 md
Reference height	250 ft
Reference length	250 ft
Reference porosity	0.45
Reference gas viscosity	0.0184 cp
Reference total compressibility	2.5×10^{-4} psi ⁻¹

$$\alpha_s = \frac{k_{f3}}{k_{fs}x_{1D}} \sqrt{\alpha_3} \tanh[\sqrt{\alpha_3}(x_{eD} - x_{1D})] + \frac{k_{f5}}{k_{fs}z_{1D}} \sqrt{c(s)}_5 \tanh[\sqrt{c(s)}_5(z_{2D} - z_{1D})] + c(s)_s \tag{91}$$

3.4.2. Damaged zone 2

For damaged zone 2, the diffusivity equation is written as

$$\frac{\partial^2 \bar{p}_{pFD3}}{\partial x_D^2} + \frac{k_{fsb}}{\frac{w_D}{2} k_{F3}} \frac{\partial \bar{p}_{pFD3}}{\partial y_D} \Big|_{y_D = \frac{w_D}{2}} - \frac{s}{\eta_{FD3}} \bar{p}_{pFD3} = 0, \tag{92}$$

where k_{fsb} is the bulk secondary fracture permeability defined by (Apaydin et al., 2012)

$$k_{fsb} = k_{fs} \frac{V_f}{V_f + V_m} = k_{fs} \frac{4\pi r_m^2 h_f / 2}{4\pi r_m^2 h_f / 2 + 4\pi r_m^3 / 3} = \frac{3k_{fs} h_f}{3h_f + 2r_m} \tag{93}$$

The no-flow boundary condition at the fracture tip is

$$\frac{\partial \bar{p}_{pFD3}}{\partial x_D} \Big|_{x_D = x_{1D}} = 0. \tag{94}$$

And the pressure continuity condition between damaged zone 2 and the propped zone is given by

$$\bar{p}_{pFD3} \Big|_{x_D = x_{FD2}} = \bar{p}_{pFD2} \Big|_{x_D = x_{FD2}} \tag{95}$$

Solving Eqs. (92)-(95) gives the solution of damaged zone 2

$$\frac{\partial \bar{p}_{pFD3}}{\partial x_D} \Big|_{x_D = x_{FD2}} = -\bar{p}_{pFD2} \Big|_{x_D = x_{FD2}} \sqrt{\alpha_{F3}} \tanh[\sqrt{\alpha_{F3}}(x_{1D} - x_{FD2})], \tag{96}$$

where

$$\alpha_{F3} = \frac{s}{\eta_{FD3}} - \frac{k_{fsb}}{\frac{w_D}{2} k_{F3}} \beta_2. \tag{97}$$

3.4.3. Propped zone

Similarly, for the propped zone, the diffusivity equation is expressed by

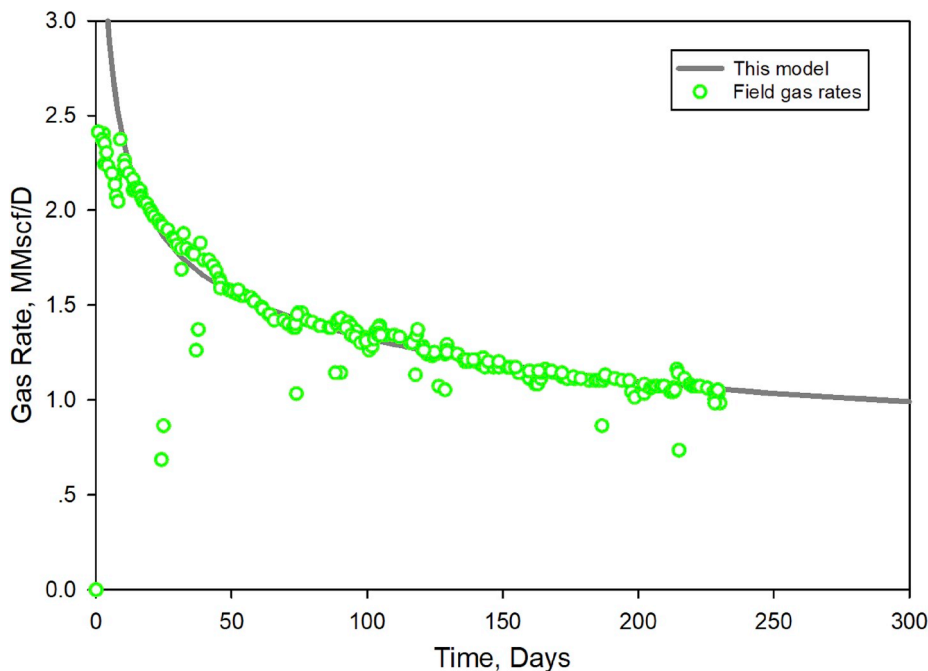


Fig. 26. Comparison between analytically simulated rates and historical data from the Marcellus-shale well.

as completely unsuccessful and no further analyses are required.

4. Discussion of the results

This section focuses on discussing the impacts of SRV properties and fracture damage on pressure and rate responses through a set of sensitivity cases. The impacts of the SRV fractal exponent and the SRV size with undamaged fractures are first analyzed. Then, single and multiple fracture damage mechanisms are added and new type curves with distinct flow regimes caused by specific fracture damage are documented. In sensitivity analyses, the undamaged hydraulic fracture permeability and USRV secondary fracture permeability are 10000 md and 30 md respectively. Hydraulic fractures are fully penetrating the reservoir in the vertical direction unless we analyze the influence of SRV height in specific cases. In SRVs, the maximal secondary fracture permeability near the fracture face is 2000 md. Finally, this model is applied to a Marcellus Shale field example with significant skin effects (Nobakht and Clarkson, 2012), which further confirms the reliability and validity of this model.

4.1. Effects of SRV properties

The power-law permeability variation is employed to describe the intrinsic secondary fracture permeability distribution along the flow direction (y -direction) due to the decreasing stimulation intensity within SRVs. For fracture networks (or SRVs), the fractal exponent is from 0 to 0.5 according to Acuna et al. (1995). Fig. 7 shows the variation of SRV secondary fracture permeability along the y -direction with different fractal exponents. It can be seen that the permeability decreases along the y -direction. When the fractal exponent is small ($\theta = 0.01$), only marginal drops in secondary fracture permeability can be observed. With the fractal exponent increases, the permeability reduction along the y -direction becomes more noticeable. And the permeability drops faster in the near-fracture areas ($y < 20$ ft). It is worth noting that the SRV half-width here is 125 ft and the secondary fracture permeability at $y = 125$ ft is still larger than that of USRVs (30 md). Fig. 8 depicts the influence of the fractal exponent on transient pressure responses. When the fractal exponent increases from 0 to 0.25, the average SRV secondary fracture permeability decreases from 2000 md to around 250 md. The pressure values become obviously larger from the matrix-fracture inter-porosity flow regime to the end of the compound linear flow regime. However, this dramatic permeability reduction only affects the concave matrix-fracture transient regime in the derivative curve. This is because the SRV secondary fracture permeability is still considerably larger than the USRV fracture permeability (30 md) at $\theta = 0.25$. And it does not significantly affect the later secondary fracture property dominated regimes. When the fractal exponent further increases to 0.5, the average SRV fracture permeability is close to the USRV fracture permeability. Both the pressure and derivative go up except those in the fracture linear flow regime and the boundary dominant regime. Fig. 9 shows that with θ increases, the secondary fracture permeability of SRVs decreases, resulting in a rate reduction after the fracture linear flow regime and a later arrival of the boundary-flow regime.

Then, the SRV width, length, and height are changed respectively to investigate the impacts of the SRV size at constant θ (0.25). As shown in Figs. 10 and 12, an increasing in the SRV size lowers the pressure and derivative from the end of the matrix-fracture transient regime to the beginning of the boundary flow. And this influence is more observable when the SRV is relatively small. In this model, raising the SRV width contributes more to the increment of the SRV because the SRV length is larger than its width. In damaged zone 3 (thickness 0.01 ft), the secondary fracture permeability is also 2000 md because fracture damage is not considered in Figs. 10–15. Similarly, as shown in Figs. 11 and 13, the late-time rate responses are more sensitive to the increment in SRV width when the SRV size is relatively small. In contrast, the variation of SRV height mainly controls early to mid-time flow regimes. Figs. 14 and

15 demonstrate that the increasing of SRV height reduces pressure and derivative values and enhances productivity from the fracture linear flow regime to the end of the bilinear flow regime. This is because when we change the SRV width, the hydraulic fracture geometry and its adjacent region remain unchanged. And if the SRV height varies, the hydraulic fracture height will also change resulting in earlier influences.

4.2. Effects of fracture conductivity damage

As mentioned earlier, four possible fracture damage scenarios are considered in this study. Fig. 16 displays the comparison among the undamaged and different-level choked fracture damage cases. It is shown that the existence of the choked section remarkably raises both pressure and derivative values in certain regimes. When the residual permeability of the damaged near-wellbore section is lower, the duration of this effect turns longer. In the heaviest damage case ($0.01k_{F1}$), the original transient bilinear and compound linear flow regimes of Fig. 6 are replaced by a new transient concave regime before the arrival of the boundary flow. For rate responses, as shown in Fig. 17, the production rates move down parallelly when severer choked damage occurs except for those near the boundary flow regime. And in the heaviest damage case, boundary flow's arrival is delayed.

Figs. 18 and 20 show the effects of partially propped or unpropped sections within hydraulic fractures on pressure responses. Particularly, we also consider the possible partially propped or unpropped section (length 200 ft, $x_{F1} = 100$ ft, $x_{F2} = 300$ ft) in the middle of the hydraulic fracture (length 400 ft) as shown in Fig. 18. This damage dominates the pressure behavior from the mid-to-late time matrix-fracture transient regime to the end of the compound linear flow regime. And the increments of pressure and derivative caused by the fracture conductivity reduction become more noticeable after the concave transient regime. However, when the damaged section (length 200 ft, $x_{F2} = 200$ ft, $x_F = 400$ ft) is located at the fracture tail, the overall influence of this damage is smaller, as shown in Fig. 20. Because it is a log-log type curve, the duration of this effect is relatively long. By comparing Figs. 18 and 20, one can conclude that the damage in the middle of a hydraulic fracture results in a stronger influence on well performances even the fracture-tail region is undamaged, which means the undamaged tail does not contribute significantly to effective fracture length. Figs. 19 and 21 depict that the productivity is higher from the late matrix-fracture transient regime to the fracture interference regime but drops faster later with the reduction of conductivity damage. Moreover, in the heaviest damage case, the duration of the fracture interference regime is longer.

4.3. Effects of fracture face damage

Figs. 22 and 23 compare the performances of the undamaged case and cases with various levels of fracture face damage. Note the secondary fracture permeability of damaged zone 3 is lower than that of the USRV for all damaged cases. It is found that fracture face damage controls the late fracture linear flow regime to the end of the matrix-fracture transient regime. When the damage becomes heavier, the humps of both pressure and derivative curves turn larger and the concave matrix-fracture transient regime in the derivative curve moves down. For rate curves, the influence of fracture face damage becomes more noticeable when the residual permeability is lower than 1% of the undamaged one. And this damage does not affect late-time performances.

4.4. Effects of multiple damage

The comparison between the undamaged case and the multiple damage case is shown in Figs. 24 and 25 and the multiple damage case here involves fracture face damage, choked fracture damage, and damaged fracture-tail regions. Based on the features shown in Figs. 16, 17, 22 and 23, it is easy to diagnose fracture face damage and choked

fracture damage. Nevertheless, it is difficult to detect the partially propped or unpropped section near the fracture tip directly from the two multiple damage curves. The properties of the partially propped or unpropped section can represent the effective fracture length. Thus, engineers can notice choked damage and fracture face damage from type curves with multiple damage more easily than interpret the effective fracture length.

4.5. Field case studies

Previously, the degraded model has been verified against a published seven-region linear flow model and the new model with complete features has not been implemented to interpret field data. In this part, the proposed model is utilized in the history matching of the production data from the Marcellus Shale (Nobakht and Clarkson, 2012). The well is a 5000-ft MFHW with 10 equally spaced hydraulic fractures producing under a constant-pressure condition. The reservoir and MFHW properties are summarized in Table 2. The SRV size (y_1 , x_f) is calculated from the fracture complexity index (FCI) which is defined as the ratio of fracture network width to its length (Cipolla et al., 2008). According to Cipolla et al. (2008), the FCI normally ranges from 0.1 to 0.5. In this model, the hydraulic fracture length is equal to the fracture network length. As the actual SRV size is unknown, we assume the SRV width (250 ft) is half the fracture spacing (500 ft) with an FCI of 0.24. The matrix intrinsic permeability given in the literature is 90 nd. Therefore, the input matrix pore radius of this model is 2.3×10^{-8} ft (corresponding matrix intrinsic permeability 93 nd). It is also worth noting that the water saturation is 24% and the effective porosity for the gas flow within the matrix consequently becomes 6.08%. Fig. 26 exhibits the matching results with a reasonable agreement between the analytical computation results and the actual gas rates. The natural and hydraulic fracture properties are estimated from the field case. Choked fracture damage and fracture face damage are identified, which is in accordance with the description of the significant amount of skin of this case in the literature. In this well-matched case, the estimated choked section within the hydraulic fracture is 33 ft with a 99.2% conductivity reduction. The estimated thickness of the impaired fracture face is 0.01 ft with a 99% permeability reduction.

5. Conclusions

In this paper, we present a new analytical model for MFHWs in shale

Appendix. Derivation and verification of the modified Langmuir adsorption equation

According to Atkins and De Paula (2009), the following relation can be obtained for ideal gas

$$pV = \frac{1}{3} nMv_{rms}^2 = nRT, \quad (\text{A-1})$$

where n is the gas amount in mol; v_{rms} is the root-mean-square speed. Similarly, the following relationship for the real gas can be obtained

$$pV = \frac{1}{3} nMv_{crms}^2 = ZnRT, \quad (\text{A-2})$$

where v_{crms} is the real-gas Z-factor corrected root-mean-square speed. Combining Eqs. (A-1) and (A-2) yields

$$v_{crms} = \sqrt{\frac{3ZRT}{M}}. \quad (\text{A-3})$$

The relationship between the mean molecular speed and the root-mean-square speed is expressed by Atkins and De Paula (2009)

$$\bar{v} = \sqrt{\frac{8}{3\pi}} v_{crms} = \sqrt{\frac{8ZRT}{\pi M}}. \quad (\text{A-4})$$

Therefore, Eq. (27) is obtained. In fact, the Langmuir equation is a function of the mean molecular speed. Let we follow the derivation of Langmuir (1918) to derive Eq. (28). When the gas is in equilibrium at the shale nano-pore surface, the rate of gas condensation on the nanopore surface is $u\alpha_c\theta$,

gas reservoirs with SRVs and damaged hydraulic fractures. This approach is verified against a published analytical model and field production data. The solutions shown here are applicable for analytical computation of well responses of general shale gas formations. On the basis of this research, the following key conclusions can be drawn:

- (1) The existence of the SRV can be a possible reason that makes the type curve deviate from those of homogeneous dual-porosity shale reservoirs. The larger the SRV fractal exponent is, the heavier the SRV secondary fracture permeability drop occurs along the y-direction and the permeability decreases faster near the hydraulic fracture. The variation of the SRV fractal exponent with large values affects more flow regimes than the variation of the SRV width and length. The response from the variation of SRV height is significantly different compared with changing its width and length.
- (2) The dominant periods of fracture face damage range from the late fracture linear flow regime to the end of the matrix-fracture transient regime. Choked fractures cause the most serious influences on the early-to-mid time pressure and rate responses. And the partially propped fractures affect the regimes between the mid-time matrix fracture transient regime and the boundary flow regime. Choked damage and partially propped sections can influence the arrival of the boundary-dominated regime. Both choked fractures and fracture face damage can be easily identified from the type curve of the multiple fracture damage case.
- (3) The model that accounts for both the SRV and the complex fracture damage is applicable for conducting the history matching of field data. Detailed high-quality input parameters, such as the SRV size and the fractal exponent, can improve the interpretation accuracy of reservoir and fracture properties.

Acknowledgments

The authors would like to acknowledge the support of UWA China Scholarships, the China Scholarship Council (CSC No. 201707970011), and the Australian Government Research Training Program (RTP) Scholarships.

where u is the number of free-gas molecules that strike the pore surface per unit time per unit surface area (the molecule-wall collision frequency per unit surface area); α_c is the fraction of molecules that strike the pore surface and then are held by the surface force; and θ is the ratio of the bare surface area to the total surface area. The adsorption on the nanopore surface only happens in the bare surface area and gas evaporation only occurs in the surface area that is completely covered by the adsorbed gas molecules. The molecule-wall collision frequency in the molar unit per unit surface area (mol/s/m^2) can be expressed by [Thompson and Owens \(1975\)](#); [Tan \(2014\)](#).

$$u = \frac{1}{4} \frac{C_n}{N_A} \bar{v} = \frac{1}{4} \frac{p}{ZRT} \bar{v} = \frac{p}{\sqrt{2\pi MZRT}} \tag{A-5}$$

where N_A is the Avogadro constant. The rate of gas evaporation can be expressed by $\nu_e \theta_1$, where ν_e is the rate of gas evaporation on the surface that is completely covered by gas molecules in mol/s/m^2 ; and θ_1 is the ratio of the surface area covered by adsorbed gas molecules to the total surface area. Therefore, in the equilibrium state, the rate of gas adsorption on the surface equals the rate of gas evaporation

$$u \alpha_c \theta = \nu_e \theta_1, \tag{A-6}$$

and

$$\theta + \theta_1 = 1. \tag{A-7}$$

Substituting Eq. (A-6) into (A-7) yields

$$\theta_1 = \frac{\alpha_c u}{\nu_e + \alpha_c u} = \frac{\frac{p}{\sqrt{2\pi MZRT}}}{\frac{\nu_e}{\alpha_c} + \frac{p}{\sqrt{2\pi MZRT}}} = \frac{\frac{p}{\sqrt{Z}}}{\sqrt{2\pi MRT} \frac{\nu_e}{\alpha_c} + \frac{p}{\sqrt{Z}}}. \tag{A-8}$$

By defining $p_L = \sqrt{2\pi MRT} \frac{\nu_e}{\alpha_c}$ in Pa, we finally have

$$\theta_1 = \frac{p/\sqrt{Z}}{p/\sqrt{Z} + p_L}, \tag{A-9}$$

$$V_{Esc} = V_L \frac{p/\sqrt{Z}}{p/\sqrt{Z} + p_L}. \tag{A-10}$$

The following two figures compared the modified model, the original model, as well as the ideal-gas model. The experimental data are from sample 2 of [Yu et al. \(2016\)](#). It is found that under a high-temperature condition (350 °F, Fig. A-1), the original and modified real-gas models match well with experimental results. For a lower temperature condition (150 °F, the field case), the revised model results fall between two boundaries drawn by the ideal-gas model and the previous real gas model, as shown in Fig. A-2.

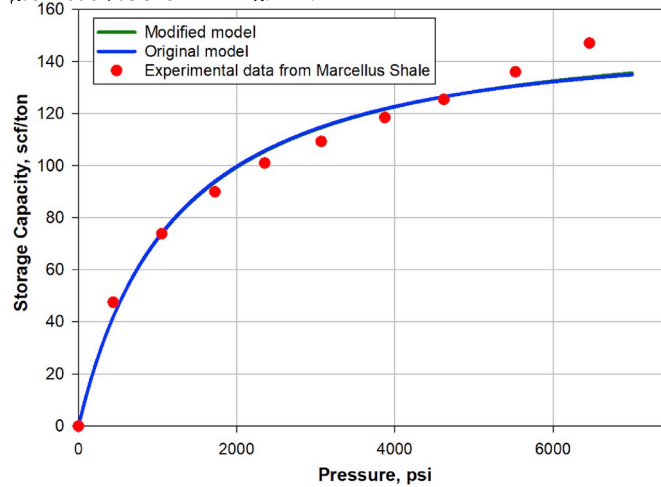


Fig. A 1. Comparison of experimental data ([Yu et al., 2016](#)) and the real-gas adsorption models.

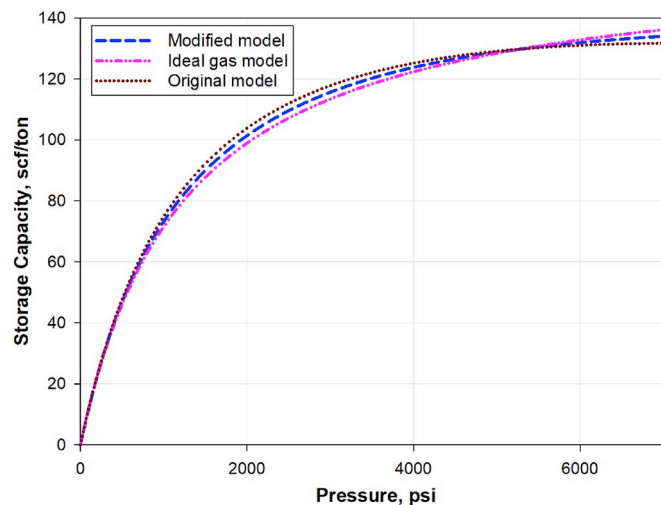


Fig. A 2. Comparison of the three models under the field case temperature.

Appendix A. Supplementary data

Supplementary data to this article can be found online at <https://doi.org/10.1016/j.petrol.2019.106686>.

References

- Acuna, J.A., Ershaghi, I., Yortsos, Y.C., 1995. Practical application of fractal pressure transient analysis of naturally fractured reservoirs. *SPE Form. Eval.* 10 (03), 173–179. <https://doi.org/10.2118/24705-PA>. SPE-24705-PA.
- Al-Hussainy, R., Ramey Jr., J.H., 1966. Application of real gas flow theory to well testing and deliverability forecasting. *J. Pet. Technol.* 18 (05), 637–642. <https://doi.org/10.2118/1243-B-PA>. SPE-1243-B-PA.
- Anderson, D.M., Mattar, L., 2007. An improved pseudo-time for gas reservoirs with significant transient flow. *J. Can. Pet. Technol.* 46 (07), 49–54. <https://doi.org/10.2118/07-07-05>.
- Apaydin, O.G., Ozkan, E., Raghavan, R., 2012. Effect of discontinuous microfractures on ultratight matrix permeability of a dual-porosity medium. *SPE Reservoir Eval. Eng.* 15 (04), 473–485. <https://doi.org/10.2118/147391-PA>. SPE-147391-PA.
- Atkins, P., De Paula, J., 2009. *Elements of Physical Chemistry*, fifth ed. Oxford University Press, USA.
- Azari, M., Soliman, M.Y., Wooden, W.O., Hunt, J.L., 1991. Performance prediction for finite-conductivity vertical fractures. Presented at the SPE Annual Technical Conference and Exhibition, Dallas, Texas. <https://doi.org/10.2118/22659-MS>, 6–9 October.
- Beskok, A., Karniadakis, G.E., 1999. Report: a model for flows in channels, pipes, and ducts at micro and nano scales. *Microscale Thermophys. Eng.* 3 (1), 43–77.
- Chang, J., Yortsos, Y.C., 1990. Pressure transient analysis of fractal reservoirs. *SPE Form. Eval.* 5 (01), 31–38. <https://doi.org/10.2118/18170-PA>. SPE-18170-PA.
- Cinco-Ley, H., Samaniego, V., 1977. Effect of wellbore storage and damage on the transient pressure behavior of vertically fractured wells. In: Presented at the SPE Annual Fall Technical Conference and Exhibition, Denver, Colorado, 9–12 October. <https://doi.org/10.2118/6752-MS>. SPE-6752-MS.
- Cinco-Ley, H., Samaniego, F., 1981. Transient pressure analysis: finite conductivity fracture case versus damaged fracture case. In: Presented at the SPE Annual Technical Conference and Exhibition, San Antonio, Texas, 4–7 October. <https://doi.org/10.2118/10179-MS>. PE-10179-MS.
- Cipolla, C.L., Warpinski, N.R., Mayerhofer, M.J., Lolon, E., Vincent, M.C., 2008. The relationship between fracture complexity, reservoir properties, and fracture treatment design. In: Presented at the SPE Annual Technical Conference and Exhibition, Denver, Colorado, USA, 21–24 September. <https://doi.org/10.2118/115769-MS>. SPE-115769-MS.
- Civan, F., Devegowda, D., Sigal, R.F., 2013. Critical evaluation and improvement of methods for determination of matrix permeability of shale. In: Presented at the SPE Annual Technical Conference and Exhibition, New Orleans, Louisiana, USA, 30 September–2 October. <https://doi.org/10.2118/166473-MS>. SPE-166473-MS.
- de Swaan, O.A., 1976. Analytic solutions for determining naturally fractured reservoir properties by well testing. *SPE J.* 16 (03), 117–122. <https://doi.org/10.2118/5346-PA>. SPE-5346-PA.
- Ertekin, T., King, G.A., Schwerer, F.C., 1986. Dynamic gas slippage: a unique dual-mechanism approach to the flow of gas in tight formations. *SPE Form. Eval.* 1 (01), 43–52. <https://doi.org/10.2118/12045-PA>. SPE-12045-PA.
- Fan, D., Etehadtavakol, A., 2017. Semi-analytical modeling of shale gas flow through fractal induced fracture networks with microseismic data. *Fuel* 193, 444–459. <https://doi.org/10.1016/j.fuel.2016.12.059>.
- Fan, D., Etehadtavakol, A., 2017. Analytical model of gas transport in heterogeneous hydraulically-fractured organic-rich shale media. *Fuel* 207, 625–640. <https://doi.org/10.1016/j.fuel.2017.06.105>.
- Guo, J., Liu, Y., 2012. Modeling of proppant embedment: elastic deformation and creep deformation. In: Presented at the SPE International Production and Operations Conference & Exhibition, Doha, Qatar, 14–16 May. <https://doi.org/10.2118/157449-MS>. SPE-157449-MS.
- Guo, J., Liu, Y., 2014. A comprehensive model for simulating fracturing fluid leakoff in natural fractures. *J. Nat. Gas Sci. Eng.* 21, 977–985. <https://doi.org/10.1016/j.jngse.2014.10.020>.
- Han, J., Wang, J.Y., 2014. Fracture conductivity decrease due to proppant deformation and crushing, a parametrical study. In: Presented at the SPE Eastern Regional Meeting, Charleston, WV, USA, 21–23 October. <https://doi.org/10.2118/171019-MS>. SPE-171019-MS.
- Jennings, S.G., 1988. The mean free path in air. *J. Aerosol Sci.* 19 (2), 159–166.
- LaFollette, R.F., Carman, P.S., 2010. Proppant diagenesis: results so far. In: Presented at the SPE Unconventional Gas Conference, Pittsburgh, Pennsylvania, USA, 23–25 February. <https://doi.org/10.2118/131782-MS>. SPE-131782-MS.
- Langmuir, I., 1918. The adsorption of gases on plane surfaces of glass, mica and platinum. *J. Am. Chem. Soc.* 40 (9), 1361–1403.
- Liu, Y., Wang, J., Guo, J., Zhu, H., Zeng, J., 2018. Numerical modeling of the conductivity of the particle monolayer with reduced size. *Geofluids*. <https://doi.org/10.1155/2018/7073091>, 2018.
- Mayerhofer, M.J., Lolon, E., Warpinski, N.R., Cipolla, C.L., Walser, D.W., Rightmire, C. M., 2010. What is stimulated reservoir volume? *SPE Prod. Oper.* 25 (01), 89–98. <https://doi.org/10.2118/119890-PA>. SPE-119890-PA.
- Miao, Y., Zhao, C., Wu, K., Li, X., 2019. Analysis of production prediction in shale reservoirs: influence of water film in inorganic matter. *J. Nat. Gas Sci. Eng.* 63, 1–9.
- Michel Villazon, G.G., Sigal, R.F., Civan, F., Devegowda, D., 2011. Parametric investigation of shale gas production considering nano-scale pore size distribution, formation factor, and non-Darcy flow mechanisms. In: Presented at the SPE Annual Technical Conference and Exhibition, Denver, Colorado, USA, 30 October–2 November. <https://doi.org/10.2118/147438-MS>. SPE-147438-MS.
- Mittal, A., Rai, C.S., Sondergeld, C.H., 2018. Proppant-conductivity testing under simulated reservoir conditions: impact of crushing, embedment, and diagenesis on long-term production in shales. *SPE J.* 23 (04), 1304–1315. <https://doi.org/10.2118/191124-PA>. SPE-191124-PA.
- Ning, X., Marcinew, R.P., Olsen, T.N., 1995. The impact of fracturing-fluid cleanup and fracture-face damage on gas production. In: Presented at the Annual Technical Meeting, Calgary, Alberta, 7–9 June. <https://doi.org/10.2118/95-43>. PETSOC-95-43.
- Nobakht, M., Clarkson, C.R., 2012. A new analytical method for analyzing linear flow in tight/shale gas reservoirs: constant-flowing-pressure boundary condition. *SPE Reserv. Eval. Eng.* 15 (03), 370–384. <https://doi.org/10.2118/143989-PA>. SPE-143989-PA.
- Ozkan, E., Raghavan, R., Apaydin, O.G., 2010. Modeling of fluid transfer from shale matrix to fracture network. In: Presented at the SPE Annual Technical Conference and Exhibition, Florence, Italy, 19–22 September. <https://doi.org/10.2118/134830-MS>. SPE-134830-MS.

- Parker, M., Weaver, J., Van Batenburg, D., 1999. Understanding proppant flowback. In: Presented at the SPE Annual Technical Conference and Exhibition, Houston, Texas, 3-6 October. <https://doi.org/10.2118/56726-MS>. SPE-56726-MS.
- Pope, C., Peters, B., Benton, T., Palisch, T., 2009. Haynesville shale - one operator's approach to well completions in this evolving play. In: Presented at the SPE Annual Technical Conference and Exhibition, New Orleans, Louisiana, 4-7 October. <https://doi.org/10.2118/125079-MS>. SPE-125079-MS.
- Qin, J., Cheng, S., He, Y., Wang, Y., Feng, D., Li, D., Yu, H., 2018. An innovative model to evaluate fracture closure of multi-fractured horizontal well in tight gas reservoir based on bottom-hole pressure. *J. Nat. Gas Sci. Eng.* 57, 295–304. <https://doi.org/10.1016/j.jngse.2018.07.007>.
- Reinicke, A., Blöcher, G., Zimmermann, G., Huenges, E., Dresen, G., Stanchits, S., et al., 2013. Mechanically induced fracture-face skin—insights from laboratory testing and modeling approaches. *SPE Prod. Oper.* 28 (01), 26–35. <https://doi.org/10.2118/144173-PA>. SPE-144173-PA.
- Romero, D.J., Valko, P.P., Economides, M.J., 2003. Optimization of the productivity index and the fracture geometry of a stimulated well with fracture face and choke skins. *SPE Prod. Facil.* 18 (01), 57–64. <https://doi.org/10.2118/81908-PA>. SPE-81908-PA.
- Song, W., Yao, J., Li, Y., et al., 2016. Apparent gas permeability in an organic-rich shale reservoir. *Fuel* 181, 973–984. <https://doi.org/10.1016/j.fuel.2016.05.011>.
- Stalgorova, K., Mattar, L., 2013. Analytical model for unconventional multifractured composite systems. *SPE Reserv. Eval. Eng.* 16 (03), 246–256. <https://doi.org/10.2118/162516-PA>. SPE-162516-PA.
- Tan, Z., 2014. *Air Pollution and Greenhouse Gases: from Basic Concepts to Engineering Applications for Air Emission Control*. Springer.
- Themig, D., 2010. Advances in OH multistage fracturing systems - a return to good fracturing practices? *J. Pet. Technol.* 62 (05), 26–29. <https://doi.org/10.2118/0510026-JPT>.
- Thompson, S.L., Owens, W.R., 1975. A survey of flow at low pressures. *Vacuum* 25 (4), 151–156.
- Valko, P., Economides, M.J., 1993. Fracture height containment with continuum damage mechanics. In: Presented at the SPE Annual Technical Conference and Exhibition, Houston, Texas, 3-6 October. <https://doi.org/10.2118/26598-MS>. SPE-26598-MS.
- Wang, J., Liu, H., Wang, L., Zhang, H., Luo, H., Gao, Y., 2015. Apparent permeability for gas transport in nanopores of organic shale reservoirs including multiple effects. *Int. J. Coal Geol.* 152, 50–62. <https://doi.org/10.1016/j.coal.2015.10.004>.
- Wang, W., Shahvali, M., Su, Y., 2015. A semi-analytical fractal model for production from tight oil reservoirs with hydraulically fractured horizontal wells. *Fuel* 158, 612–618. <https://doi.org/10.1016/j.fuel.2015.06.008>.
- Wang, X., Indriati, S., Valko, P.P., Economides, M.J., 2000. Production impairment and purpose-built design of hydraulic fractures in gas-condensate reservoirs. In: Presented at the International Oil and Gas Conference and Exhibition in China, Beijing, China, 7-10 November. <https://doi.org/10.2118/64749-MS>. SPE-64749-MS.
- Wasaki, A., Akkutlu, I.Y., 2015. Permeability of organic-rich shale. *SPE J.* 20 (06), 1384–1396. <https://doi.org/10.2118/170830-PA>. SPE-170830-PA.
- Wu, K., Chen, Z., Li, X., Guo, C., Wei, M., 2016. A model for multiple transport mechanisms through nanopores of shale gas reservoirs with real gas effect—adsorption-mechanic coupling. *Int. J. Heat Mass Transf.* 93, 408–426. <https://doi.org/10.1016/j.ijheatmasstransfer.2015.10.003>.
- Wu, K., Li, X., Guo, C., Wang, C., Chen, Z., 2016. A unified model for gas transfer in nanopores of shale-gas reservoirs: coupling pore diffusion and surface diffusion. *SPE J.* 21 (05), 1–583.
- Wu, Y., Cheng, L., Huang, S., Fang, S., Jia, P., Rao, X., 2019. An analytical model for analyzing the impact of fracturing fluid-induced formation damage on rate transient behavior in tight formations. *J. Pet. Sci. Eng.* 179, 513–525.
- Yu, W., Sepehrnoori, K., Patzek, T.W., 2016. Modeling gas adsorption in Marcellus shale with Langmuir and bet isotherms. *SPE J.* 21 (02), 589–600.
- Zeng, J., Wang, X., Guo, J., Zeng, F., 2017. Composite linear flow model for multi-fractured horizontal wells in heterogeneous shale reservoir. *J. Nat. Gas Sci. Eng.* 38, 527–548. <https://doi.org/10.1016/j.jngse.2017.01.005>.
- Zeng, J., Wang, X., Guo, J., Zeng, F., Zhang, Q., 2018. Composite linear flow model for multi-fractured horizontal wells in tight sand reservoirs with the threshold pressure gradient. *J. Pet. Sci. Eng.* 165, 890–912. <https://doi.org/10.1016/j.petrol.2017.12.095>.
- Zeng, J., Wang, X., Guo, J., Zeng, F., Zeng, F., 2019. Modeling of heterogeneous reservoirs with damaged hydraulic fractures. *J. Hydrol.* 574, 774–793.